

THESIS FOR THE DEGREE OF DOCTOR OF PHILOSOPHY

High-efficiency dissipative Kerr solitons in
microresonators

Óskar Bjarki Helgason



CHALMERS

Photonics Laboratory
Department of Microtechnology and Nanoscience (MC2)
Chalmers University of Technology
Göteborg, Sweden, 2022

High-efficiency dissipative Kerr solitons in microresonators

Óskar Bjarki Helgason

©Óskar Bjarki Helgason, 2022

ISBN 978-91-7905-647-6

Doktorsavhandlingar vid Chalmers tekniska högskola,

Ny serie nr 5113

ISSN 0346-718X

Photonics Laboratory

Department of Microtechnology and Nanoscience (MC2)

Chalmers University of Technology

SE-412 96 Göteborg

Sweden

Telephone: +46 (0)31-772 10 00

Printed by Chalmers Reproservice,

Chalmers tekniska högskola,

Göteborg, Sweden, 2021

High-efficiency dissipative Kerr solitons in microresonators
Óskar Bjarki Helgason
Photonics Laboratory
Department of Microtechnology and Nanoscience (MC2)
Chalmers University of Technology

Abstract

The microresonator comb (microcomb) is a laser source that generates equally spaced coherent lines in the spectral domain. Having a chip-scale size and the potential of being low cost, it has attracted attention in multiple applications. Demonstrations have included high-speed optical communications, light detection and ranging, calibrating spectrographs for exoplanet detection and, optical clocks. These experiments typically rely on the generation of a dissipative Kerr soliton (DKS) — a temporal waveform that circulates the microresonator without changing shape. However, these DKS states have thus far been limited in certain technical aspects, such as energy efficiency, which are essential for realizing commercial microcomb solutions.

This thesis studies the dynamics of DKSs in microresonators aiming at developing a reliable and high-performing microcomb source. The investigation will cover DKSs found both in the normal and anomalous dispersion regime of silicon nitride microresonators. The performance of microcombs in terms of line power is numerically explored in single-cavity arrangements for telecommunication purposes. DKSs generated in linearly coupled microcavities are investigated, revealing exotic dynamics and improved performance in terms of power efficiency and DKS initiation. These studies facilitate reliable energy-efficient microcombs, bringing the technology a step closer to commercial use.

Keywords: nonlinear optics, dissipative solitons, dissipative Kerr solitons, microresonators, microcombs, optical frequency combs

Publications

This thesis is based on the work contained in the following papers:

- [A] Ó. B. Helgason, A. Fülöp, J. Schröder, P. A. Andrekson, A. M. Weiner and V. Torres-Company, “Superchannel engineering of microcombs for optical communications”, *Journal of the Optical Society of America B*, 36, 8, 2013-2022, 2019.
- [B] V. Torres-Company, J. Schröder, A. Fülöp, M. Mazur, L. Lundberg, Ó. B. Helgason, M. Karlsson, P. A. Andrekson, “Laser frequency combs for coherent optical communications”, *Journal of Lightwave Technology*, 37, 7, 1663-1670, 2019.
- [C] E. Nazemosadat, A. Fülöp, Ó. B. Helgason, P.-H. Wang, Y. Xuan, D. E. Leaird, M. Qi, E. Silvestre, A. M. Weiner and V. Torres-Company, “Switching dynamics of dark-pulse Kerr comb states in optical microresonators”, *Physical Review A*, 103, 013513, 2021.
- [D] Ó. B. Helgason, F. R. Arteaga-Sierra, Z. Ye, K. Twayana, P. A. Andrekson, M. Karlsson, J. Schröder and V. Torres-Company, “Dissipative Kerr solitons in photonic molecules”, *Nature Photonics*, 15, 4, 305-310, 2021.
- [E] Ó. B. Helgason, Z. Ye, J. Schröder and V. Torres-Company, “Bidirectional initiation of dissipative solitons in photonic molecules”, *Conference on Lasers and Electro-Optics Europe & European Quantum Electronics Conference (CLEO/Europe-EQEC)*, Munich, Germany, paper ef51, 2021.
- [F] Ó. B. Helgason, M. Girardi, Z. Ye, F. Lei, J. Schröder and V. Torres-Company, “Power efficient soliton microcombs”, *Preprint*, arXiv:2202.09410 .

Related publications and conference contributions by the author, not included in the thesis:

- [G] K. S. Twayana, Z. Ye, Ó. B. Helgason, K. Vijayan, M. Karlsson, V. Torres-Company “Frequency-comb-calibrated swept-wavelength interferometry”, *Optics Express*, **29**, 15, 24363-24372, 2021
- [H] K. S. Twayana, Z. Ye, Ó. B. Helgason, K. Vijayan, M. Karlsson, V. Torres-Company *Conference on Lasers and Electro-Optics Europe & European Quantum Electronics Conference (CLEO/Europe-EQEC)*, Munich, Germany, paper ed65, 2021.
- [I] D. Kong, A. A. Jørgensen, M. R. Henriksen, F. Klejs, Z. Ye, Ó. B. Helgason, H. E. Hansen, H. Hu, M. Yankov, S. Forchhammer, P. Andrekson, A. Larsson, M. Karlsson, J. Schröder, Y. Sasaki, K. Aikawa, J. W. Thomsen, T. Morioka, M. Galili, V. Torres-Company, and L. K. Oxenløwe “Single Dark-Pulse Kerr Comb Supporting 1.84 Pbit/s Transmission over 37-Core Fiber”, *Conference on Lasers and Electro-Optics (CLEO)*, San Jose, USA, paper JTh4A.7, 2020.
- [J] Ó. B. Helgason, Z. Ye, K. Twayana, P. A. Andrekson, J. Schröder and V. Torres-Company “Dark-pulse Kerr combs in linearly coupled microring structures”, *Conference on Lasers and Electro-Optics (CLEO)*, San Jose, USA, paper STu3H.5, 2020.
- [K] V. Torres-Company, J. Schröder, A. Fülöp, M. Mazur, L. Lundberg, Ó. B. Helgason, M. Karlsson and P. A. Andrekson “Laser Frequency Combs for Coherent Optical Communications”, *Journal of Lightwave Technology*, **37**, 7, 1663-1670, 2019.
- [L] Z. Ye, A. Fülöp, Ó. B. Helgason, P. A. Andrekson, and V. Torres-Company “Low-loss high-Q silicon-rich silicon nitride microresonators for Kerr nonlinear optics”, *Optics Letters*, **44**, 3326-3329, 2019.
- [M] A. Fülöp, M. Mazur, A. Lorences-Riesgo, Ó. B. Helgason, P.-H. Wang, Y. Xuan, D. E. Leaird, M. Qi, P. A. Andrekson, A. M. Weiner and V. Torres-Company “Low-loss high-Q silicon-rich silicon nitride microresonators for Kerr nonlinear optics”, *Nature Communications*, **9**, 1598, 2018.

- [N] E. Nazemosadat, A. Fülöp, Ó. B. Helgason, P.-H. Wang, Y. Xuan, D. E. Leaird, M. Qi, E. Silvestre, A. M. Weiner, and V. Torres-Company “Hot-Cavity Spectroscopy of Dark Pulse Kerr Combs in Microresonators”, *Conference on Lasers and Electro-Optics Europe & European Quantum Electronics Conference (CLEO/Europe-EQEC)*, Munich, Germany, paper ed65, 2019.
- [O] E. Nazemosadat, A. Fülöp, Ó. B. Helgason, P.-H. Wang, Y. Xuan, D. E. Leaird, M. Qi, E. Silvestre, A. M. Weiner, and V. Torres-Company “Switching Dynamics of Dark Solitons in Kerr Microresonators”, *Conference on Lasers and Electro-Optics Europe & European Quantum Electronics Conference (CLEO/Europe-EQEC)*, Munich, Germany, paper ef84, 2019.
- [P] Z. Ye, A. Fülöp, Ó. B. Helgason, P. A. Andrekson, V. Torres-Company “Low loss silicon-rich silicon nitride for nonlinear optics”, *Conference on Lasers and Electro-Optics (CLEO)*, San Jose, USA, 2018
- [Q] Ó. B. Helgason, A. Fülöp, J. Schröder, P. A. Andrekson, A. M. Weiner, V. Torres-Company “Superchannel engineering with microresonator combs”, *Conference on Lasers and Electro-Optics (CLEO)*, San Jose, USA, 2018

Contents

Abstract	iii
Publications	v
Acknowledgement	xi
Acronyms	xiii
1 Introduction	1
1.1 This thesis	4
1.1.1 Thesis outline	5
2 Solitons and nonlinear propagation	7
2.1 Optical propagation in nonlinear dielectric waveguides . . .	7
2.2 Introduction to soliton dynamics	10
2.3 Dissipative solitons	11
3 Microresonators and photonic molecules	15
3.1 Characteristics of a single microring resonator	15
3.1.1 Cavity losses and Q factors	18
3.1.2 Dispersion in microresonators	20
3.2 Linear dynamics of photonic molecules	23
3.2.1 Dispersion profile of photonic molecules	24
3.2.2 Transmission response of photonic molecules	27
4 Soliton generation in microresonators	33
4.1 Nonlinear dynamics in a single cavity	33
4.1.1 The Lugiato-Lefever equation	34
4.1.2 Bistability	35
4.1.3 Modulational instability	36

4.2	DKS generation in microresonators	40
5	Nonlinear dynamics in photonic molecules	45
5.1	Power buildup in Kerr-nonlinear photonic molecules . . .	46
5.2	Replacing the auxiliary cavity with a constant frequency shift	48
5.3	DKS initiation in the normal dispersion regime	49
6	Future outlook	53
7	Summary of Papers	55
	Included papers A–F	91

Acknowledgement

I have been lucky to have had a long list of people who have supported me through my PhD journey. My partner, Pórdís, and two daughters, Sigurlaug and Andrea, belong at the top of this list for their love and patience during this time.

I am most grateful for the support from my supervisor, Prof. Victor Torres-Company. His guidance has certainly been the key element in helping me learn and grow as a researcher. I am grateful to Dr. Jochen Schröder for valuable support and guidance. I also thank Prof. Peter Andrekson and Prof. Magnus Karlsson for sharing helpful knowledge and insights.

The Ultrafast Photonics Laboratory consists of wonderful people that I thoroughly enjoy working with. I am thankful to all of them for how ready they have been to help and discuss things over the years. I am especially grateful to Dr. Attila Fülöp for giving up so much of his time to teach me about microcombs and laboratory work. I thank Zhichao Ye and Marcello Girardi for fruitful discussions and for making excellent microrings that have boosted the value of my research. I appreciate having a great office mates in Dr. Fransisco Arteaga-Sierra and Dr. Fuchuan Lei. I thank Israel Rebolledo Salgado and Krishna Twayana for enduring countless excessively long conversations with me about microcombs, lab work and other topics.

I would like to thank everyone in the Photonics Laboratory for all the help and fun I have had with them. A special thanks goes to Alexander Grabowski and Dr. Lars Lundberg for all the support and help throughout the PhD. I also thank Connor Skehan, Dr. Elham Nazemosadat, Asbjørn Jørgensen, Prof. Andrew Weiner and others for excellent collaborations.

Acronyms

CMOS	complementary metal–oxide–semiconductor
CW	continuous wave
DS	dissipative soliton
DKS	dissipative Kerr soliton
EDFA	erbium-doped fiber amplifier
EOC	electro-optic comb
FSR	free spectral range
FWHM	full width at half maximum
FWM	four-wave mixing
GVD	group velocity dispersion
LLE	Lugiato-Lefever equation
MI	modulation instability
Microcomb	microresonator frequency comb
MLL	mode-locked laser
NLSE	nonlinear Schrödinger equation
OFC	optical frequency comb
OSA	optical spectrum analyzer
RF	radio frequency
SPM	self-phase modulation
VNA	vector network analyzer
WDM	wavelength-division multiplexing
XPM	cross-phase modulation

Chapter 1

Introduction

In 2005, John L. Hall and Theodore W. Hänsch shared half of the Nobel prize in physics for their contributions to precision spectroscopy [1, 2]. Their work in the late 90s and early 2000s would lead to dramatic improvements to atomic clocks [3, 4], but a key element to their success was the development of an optical frequency comb (OFC).

In contrast to the continuous wave (CW) laser, which outputs light at a single discrete frequency, an OFC is a laser source that outputs a discrete series of equally spaced lines in the frequency domain [5]. A critical feature of these comb lines is that they have a fixed phase relationship with each other. As such, they typically correspond to a train of optical pulses in the time domain, with a repetition rate (f_{rep}) equal to the comb line separation. The absolute optical frequency of each comb line (f_n) is represented by $f_n = nf_{rep} + f_{ceo}$, where f_{ceo} stands for carrier-envelope offset frequency, caused by a constant phase slippage between consecutive pulses. Thus, the absolute frequency of each comb line can be determined if both f_{rep} and f_{ceo} are known.

While f_{rep} is usually easily measured as a radio frequency (RF) beat-note between comb lines, measuring f_{ceo} comprises a considerable challenge, which was one of the main achievements of the Nobel awarded OFC. It required an octave-spanning comb spectrum, accomplished by broadening a mode-locked laser (MLL) via the Kerr effect in a highly nonlinear fiber (HNLF). By implementing a self-referencing technique, the f_{ceo} of the octave-spanning comb was made available as an RF beat-note [6] such that the absolute frequency of each comb line could be determined and stabilized with remarkable precision. Utilizing the comb lines as a series of optical references, this enabled the determination of

optical frequencies with orders of magnitude higher precision and lower hardware complexity compared to previous technologies, facilitating the development of optical clocks [7].

The research field of OFCs has since expanded at an incredible rate. OFCs are now studied within multiple application domains, e.g. as an astrocomb [8], where a spectrograph calibrated with an OFC captures the Doppler shift of stars for exoplanet detection; for dual-comb spectroscopy [9], a technique useful both for spectroscopy and light detection and ranging (LIDAR) where two OFC combs are used to map an optical spectrum onto a narrower RF spectrum; in RF photonics [10], e.g. to generate low noise microwave signals; and in optical telecommunications [11], replacing multiple CW lasers for carrier generation and enabling enhancements in terms of spectral efficiency and signal processing. Note that the need for self-referencing, and the optimal comb characteristics in general, varies on a case by case basis. For example, atomic clocks require self-referencing with high stability and an octave-spanning spectrum [6, 12]. In contrast, optical telecommunications require a relatively narrow and flat spectrum with high line power [11].

Different sources can be employed as an OFC. One is the MLL, which generates synchronized optical pulses by periodically introducing absorption to a laser cavity, where the line spacing of the generated OFC is defined by the length of the laser cavity [13]. Having existed since the early 60's [14], the MLL is well established and commercially available. The electro-optic comb (EOC) is another OFC source which is easily assembled using commercially available components primarily developed for telecommunications. It is generated by modulating a CW laser with an RF tone via electro-optic modulation (EOM), typically using a cascade of phase and intensity modulators [15]. It is flexible in terms of tunability since the center frequency can be changed by tuning the wavelength of the laser and the line spacing can be changed by tuning the frequency of the RF tone. The spectrum can be broadened to an octave in a highly nonlinear fiber, but excess phase noise originating from the RF clock is often an obstacle for self-referencing. Recent experiments have overcome this obstacle by filtering the lines of the EOC in an optical cavity, achieving self-referencing at a stability comparable to the MLL [16, 17].

With the MLL and the EOC readily available as table-top solutions, an increasing effort has been spent on realizing chip-scale OFCs [18]. Such devices promise a dramatic reduction in size with co-integration of other optical components at a potential low cost, e.g. by using fabrication

methods compatible with complementary metal–oxide–semiconductor (CMOS) processes [19]. Miniaturization enables new opportunities, especially in settings outside of the laboratory. While progress has been made in making chip-scale MLLs [20] and EOCs [21], another prominent candidate is the microresonator frequency comb (microcomb) [22, 23].

First demonstrated in the mid 2000s [24, 25], the microcomb is generated in a microresonator by employing the Kerr effect to convert input power from a CW laser to other comb lines [26]. The generated lines are confined to the resonances of the cavity, where four-wave mixing (FWM) allows energy transfer to evenly spaced and coherent comb lines. Such dynamics are in fact not limited to microresonators since larger scale cavities, such as optical fiber resonators, can also feature Kerr frequency comb generation [27, 28]. A thorough investigation into the physics of Kerr nonlinear resonators has led to the realization of coherent microcombs exhibiting several distinct intra-cavity waveforms in the form of dissipative Kerr solitons (DKSs). Among those are the anomalous DKSs [28, 29] and soliton crystals [30], both found in anomalous dispersion cavities, but also the less known normal DKS (sometimes called mode-locked dark pulse), found in normal dispersion cavities [31]. These waveforms have been used for microcomb demonstrations in applications [22], such as optical clocks [32], optical telecommunication [33–35], dual-comb spectroscopy [36, 37], distance range measurements [38, 39] and astrocombs [40].

Tremendous improvements have been made in the integration of microcombs over the last years, with DKSs demonstrated in multiple material platforms [19], such as LiNbO_3 [41], Si_3N_4 [42, 43], SiO_2 [44] and AlN [45]. Recent efforts have made crucial steps towards integrated optical systems, promising reliable co-integration of microcombs with lasers [46–48] and other optical components [49, 50]. The investigation of DKS dynamics has also led to improvements on several fronts, such as DKS initiation [51–54], low noise performance [55], high bandwidth engineering [45, 56] and low power operation [57]. Promising as these experiments were, the microcomb still requires more development to be established as a competing OFC solution.

One persisting challenge of DKSs is the limited conversion efficiency, i.e. the portion of input optical CW power converted to comb lines at other frequencies. Having low power conversion efficiency translates into lower wall-plug energy efficiency and low optical signal to noise ratio, which is unfavorable for most applications. This low efficiency is espe-

cially problematic for the DKSs in anomalous single-cavity structures, where the conversion efficiency is fundamentally limited [58]. The DKS generated in the normal dispersion regime offers much higher conversion efficiency but at the cost of a more uneven spectrum [53, 59], a characteristic not desirable for astrocombs and telecommunications. Multiple different approaches have been suggested and demonstrated, such as pulsed pumping [40, 60, 61], microresonator nesting in laser cavities [62] and Pockels microcombs [63]. Yet another architecture is to use an arrangement of linearly coupled microcavities [52, 53, 64], an arrangement which will be thoroughly analyzed for DKS generation in this thesis.

1.1 This thesis

This thesis focuses on the dynamics of microresonator frequency combs with the practical goal of realizing reliable designs with high conversion efficiency and flat spectral distribution of power. Much emphasis is put on linearly-coupled microcavities (photonic molecules) since such arrangements can enhance the dynamics of DKSs in several ways, including improved conversion efficiency and reliable initiation. For this, both simulations and experimental measurements are conducted using microrings fabricated in silicon nitride.

In Paper A, single-mode microresonators are studied, where both anomalous and normal DKSs are numerically simulated over a large parameter space in order to discover optimized designs for optical telecommunication applications.

The study in Paper B quantifies the requirements of OFCs in wavelength-division multiplexed (WDM) optical fiber links. It also features a theoretical comparison between EOCs and microcombs.

Paper C features a careful experimental and numerical investigation of the initiation process of a normal DKS from a CW laser in a single microcavity containing two linearly coupled waveguide modes.

In Paper D, power efficient microcombs are experimentally demonstrated from two linearly coupled normal-dispersion microresonators. Numerical simulations and experiments verify that a DKS circulates the main cavity. The existence regime of these microcombs is found to be considerably larger compared to the normal DKS generated in a single-mode cavity.

Paper E is a short extension to Paper D, demonstrating backwards initiation of a DKS in linearly-coupled normal-dispersion microres-

onators.

In Paper F, a single DKS is experimentally generated in an anomalous dispersion microresonator with vastly improved performance in terms of power efficiency. Such enhancements were enabled by shifting the CW pumped resonance in the microcavity through linear coupling to an auxiliary cavity. Exotic effects were also demonstrated, such as backwards initiation and DKS operation with a blue detuned pump laser.

1.1.1 Thesis outline

Chapter 2 serves as a brief introduction to the soliton dynamics in non-linear waveguides. Chapter 3 discusses the cold cavity dynamics of microresonators, both for single microcavities and linearly coupled cavities. In Chapter 4, the microcomb generation and soliton dynamics microcavities are described, while Chapter 5 discusses microcomb generation in linearly-coupled microrings. Finally, Chapter 6 is the future outlook.

Chapter 2

Solitons and nonlinear propagation

An essential part for generating DKSs in microresonators is the circulation of light through a nonlinear waveguide. For the silicon nitride waveguide considered in this thesis, such propagation has dynamics similar to optical fibers, which involves the Kerr effect and group velocity dispersion. These dynamics can be modelled using the nonlinear Schrödinger equation (NLSE). The NLSE predicts the existence of solitons in optical fibers [65], and with the right modifications, it can be used to predict the dynamics of DKSs in microresonators.

In the next section, the NLSE will be briefly introduced. It is then employed in the following two sections to describe the basic dynamics of classical solitons and dissipative solitons.

2.1 Optical propagation in nonlinear dielectric waveguides

The purpose of an optical waveguide is to spatially confine a beam of light as it is propagated from one place to another. A good example is the optical fiber, which carries data in the form of modulated light between cities and continents, forming the backbone of today's internet infrastructure [66]. Another example are the silicon nitride waveguides we use in this thesis. Such waveguides feature two dielectric materials, a core and a cladding, where the core has a higher refractive index. This refractive index difference provides the means to guide the optical

light beam along the length of the waveguide. Intuitively, we can understand this process using the ray-optics approximation, which predicts the confinement of light to the core due to total internal reflection at the dielectric boundaries. A more accurate description can be derived from Maxwell's equations, where the waveguide is found to support a finite number of waveguide modes, with each mode having a specific electric field distribution and propagation constant [67].

To model the pulse propagation in Kerr nonlinear waveguides we use the NLSE. Here, we give a brief overview of the NLSE, leaving the details of the derivation to the literature [68, 69]. The NLSE describes the evolution of a slowly varying electric field envelope (A) in a single waveguide mode (with single polarization) which is guided along the z -axis. The z -component of the electric field is typically neglected in the case of optical fibers, but it has a considerable impact in high confinement waveguide, resulting in a modified nonlinear coefficient [70]. The characteristics of the propagation appear as constants (e.g. loss, dispersion, nonlinearity) that modify the electric field envelope as a scalar. The NLSE is given by

$$\frac{\partial A}{\partial z} = i\gamma|A|^2A - \frac{\alpha}{2}A - \beta_1\frac{\partial A}{\partial t} - \frac{i\beta_2}{2}\frac{\partial^2 A}{\partial t^2}, \quad (2.1)$$

where α is the propagation loss for each unit of length, β_1 is the inverted group velocity. The group velocity dispersion (GVD) is described by β_2 , where anomalous dispersion ($\beta_2 < 0$) signifies that higher frequencies go faster than lower frequencies, while normal dispersion ($\beta_2 > 0$) signifies the opposite. The Kerr effect is depicted by the nonlinear coefficient, γ , which can manifest in several nonlinear effects, such as self-phase modulation (SPM), cross-phase modulation (XPM), and four-wave mixing (FWM). Other effects such as higher-order dispersion, the Raman effect and self-steepening have been left out of the equation above since they are not essential for the discussion in this thesis. The electric field envelope is normalized such that $|A|^2 = P$, where P is the optical power. The normalized electric field can be found as

$$E(z, t) = A(z, t)e^{i(\beta_0 z - \omega_0 t)} \quad (2.2)$$

where β_0 is the phase constant.

Because of the nonlinear term, the NLSE is not easy to analytically integrate. However, it is relatively simple to simulate. The simulations in this work will be based on either the split-step method [68] or the Runge-Kutta method in the interaction picture [71], but both methods simulate

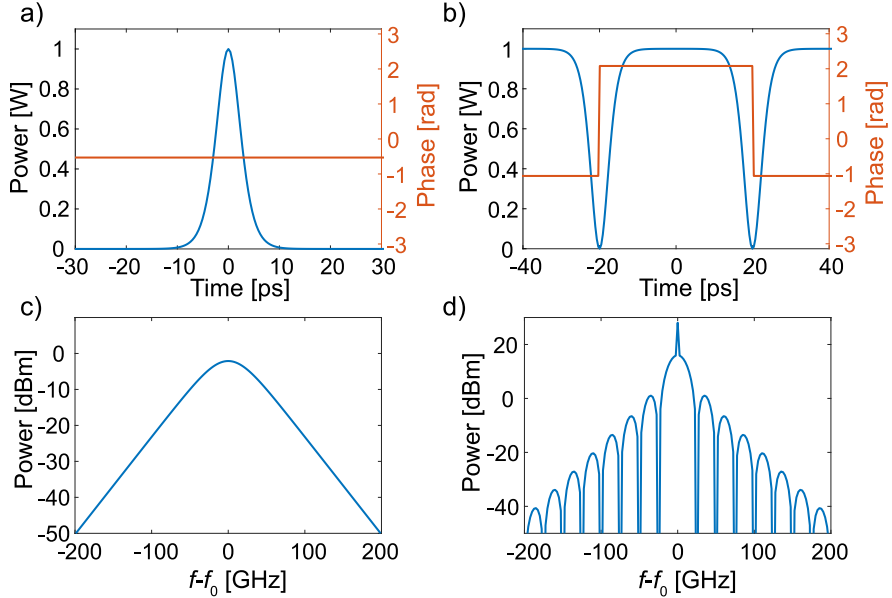


Figure 2.1: The plot in a (b) shows the temporal structure of single bright (two dark) soliton after 100 km lossless propagation in an optical fiber, i.e. the pulse is only affected by the Kerr effect and GVD ($\gamma = 0.002 (Wm)^{-1}$, $\beta_2 = \pm 20 ps^2/km$). The corresponding spectra are shown in c and d for bright and dark solitons respectively, where f is the optical frequency and $f_0 = \omega_0/2\pi$ is the center frequency of the soliton. In the simulation, these waveforms propagate without change to temporal and spectral power profiles. Note that the bright soliton features a constant phase, while the dark solitons exhibit a π phase shift. Two dark solitons are simulated to avoid simulation artifacts.

propagation by taking small enough steps such that the nonlinear and linear portion of the NLSE can be applied separately. For simplification, the β_1 is often removed from the equation by assuming a reference frame moving at group velocity.

The NLSE predicts several nonlinear phenomena, such as the spectral broadening of optical pulses [72], optical pulses emerging from a perturbed CW wave through modulational instability [73], and the balancing of GVD and Kerr nonlinearity to allow a soliton to propagate long distances [74]. Such solitons are the topic of the next section.

2.2 Introduction to soliton dynamics

Solitons were first observed as translational waves in a water canal by J.S. Russell in the early 1800s [75]. They are defined as waves that travel through time and space at a constant velocity while maintaining their shapes [76]. This first definition was based on the Korteweg-de Vries equation [77], which describes the nonlinear dispersive dynamics found in different energy conservative systems, such as shallow-water waves and plasma physics [78]. Solitons have since been found as solutions to a variety of nonlinear partial differential equations covering multiple disciplines of physics [79]. The NLSE is one such system which not only describes optical propagation in Kerr-nonlinear waveguides, but also self-focusing in Kerr nonlinear media [80] and the dynamics of deep-water waves [81, 82].

The first description of temporal solitons in optical fibers came in 1973 [74, 83], with bright solitons appearing in the anomalous dispersion regime [84], and dark solitons in the normal dispersion regime [85]. As a demonstration, we simulate examples in an optical fiber only featuring the Kerr nonlinearity and GVD (see figure 2.1), initiating the solitons from mathematical closed-form expressions [68]. These solitonic pulses propagate unchanged because of a balance between the GVD and SPM. The source of this balance is that the SPM generates a positive chirp in a negative slope of the intensity distributed pulse and a negative chirp in the positive slope of a pulse. For the bright soliton, this means that lower frequencies will appear on the leading edge, but the anomalous GVD corrects this chirp since the higher frequencies move faster. A similar story can be told about the dark soliton, only with higher frequencies appearing on the trailing edge. A key difference between these two types of solitons is the sharp phase transition at the center of the dark soliton. Thus the dark soliton requires a background with an appropriate change of phase [85, 86].

In a lossless fiber, a soliton can in principle propagate indefinitely. It was for this reason that much effort was spent on studying solitons for carrying data in fiber optical telecommunications [65]. In such systems, losses of the fiber become significant at longer distances, causing the soliton to become wider and shrink in amplitude [87]. Thus, various gain elements were often employed such that the average system would be effectively lossless while maintaining similar soliton dynamics. One of the main obstacles in these systems was the timing jitter caused by the Gordon-Haus effect [88], with the telecommunications field eventually

abandoning the solitons in favor of WDM systems [66]. Interestingly, recent studies have considered the employment of a different type of soliton — the dissipative soliton — for the generation of optical carriers in future telecommunication systems [35]. Such waveforms are the topic of the next section.

2.3 Dissipative solitons

The dissipative soliton (DS) thrives in systems which exhibit continuous energy exchange. As such, the DS is not only reliant upon a balance between nonlinearity and dispersion, but it also depends on the balance between gain and loss [89]. Much like the classical solitons, the DSs are generic structures that appear not only in optical systems [90], but also other branches of physics such as fluid mechanics [91] and plant ecology [92].

Mode-locked lasers (MLLs) can support DSs in the form of an optical temporal pulse circulating the laser cavity. Such DSs exist as a balance between the GVD, nonlinearity, amplification and cavity losses. The series of pulses coupled out of the laser cavity correspond to a frequency comb in the spectral domain. The MLL features amplification in a resonant cavity, often with other added elements such as spectral filters, saturable absorbers and a Kerr medium. As such, a wide range of MLL configurations are possible, enabling a variety of DS dynamics [90]. This includes bright and dark DS waveforms that are similar to the fiber solitons [93,94], soliton molecules [50], dissipative soliton resonances [95] and soliton explosions [96].

Kerr nonlinear resonant cavities can also maintain a DS when driven by a CW laser, for example in optical fiber cavities [28] or microresonators [29]. The gain of such DSs is supplied via parametric amplification from a CW input pump over a broad spectrum which compensates for the losses [22]. The use of the Kerr effect to supply gain is perhaps the main reason why these waveforms have become known as dissipative Kerr solitons (DKS). As such, the power of the center wavelength needs to be kept at a high enough level so that it can maintain the DKS. In the frequency domain, the DKS corresponds to a frequency comb, often named 'Kerr frequency comb'. Here, Kerr frequency combs generated in microresonators will be referred to as 'microcombs'.

DKSs are in principle not limited to CW driven cavities. Here we run a little test to demonstrate that a laser cavity can support a DKS

through saturated amplification of the center wavelength of the DKS. Figure 2.2a shows the layout of a simple cavity with such an amplifier, where the gain profile does not reach other resonant modes of the cavities. Thus, the other frequency components of the DKS have to gain energy through parametric amplification. A simulation was conducted by solving equation 2.1 ($\beta_2 = \pm 200 \text{ ps}^2/\text{km}$, $\gamma = 0.002 (\text{Wm})^{-1}$, $\alpha = 0.9 \text{ km}^{-1}$) for a full roundtrip of propagation ($L = 20 \text{ cm}$). In each roundtrip, a portion of power was coupled from the cavity ($\theta = 0.002$) and the amplifier would amplify the CW wave according to $A'(f_0) = A(f_0)e^{\frac{P_{sat}}{P_{sat} + |A(f_0)|^2} \frac{\alpha L + \theta}{}}$. Figures 2.2b-d show the generation of a dark pulse in the normal dispersion regime, with $P_{sat} = 7.4 \text{ W}$, initiating from two dark solitons similar to figure 2.1b. The anomalous DKS is displayed in figures 2.2e-g, with $P_{sat} = 1.5 \text{ W}$, and initiating from a bright soliton similar to figure 2.1a. For the anomalous DKS to stabilize, a constant phase offset of 0.0017 radians to the center wavelength was needed every roundtrip. The amplitude of the anomalous DKS waveform has a sech shape similar to the fiber soliton in figure 2.1. However, unlike the fiber soliton, the waveform also includes a CW background and a non-flat phase profile. This change in phase profile is a consequence of the interaction between frequencies through FWM [97]. The normal DKS waveform is distinctly different from its fiber soliton counter part in figure 2.1, both in phase and amplitude. It takes the form of a dark pulse carved out of a CW background with ripples at the bottom, with the phase value switching in unison with the amplitude. This type of structure has been described as an interlock between two switching waves [98].

This short analysis demonstrates the difference in dynamics between the DS and the classical soliton in figure 2.1. Furthermore, it shows that DKSs are not limited to microcavities, and can be generated in laser cavities using the right configuration.

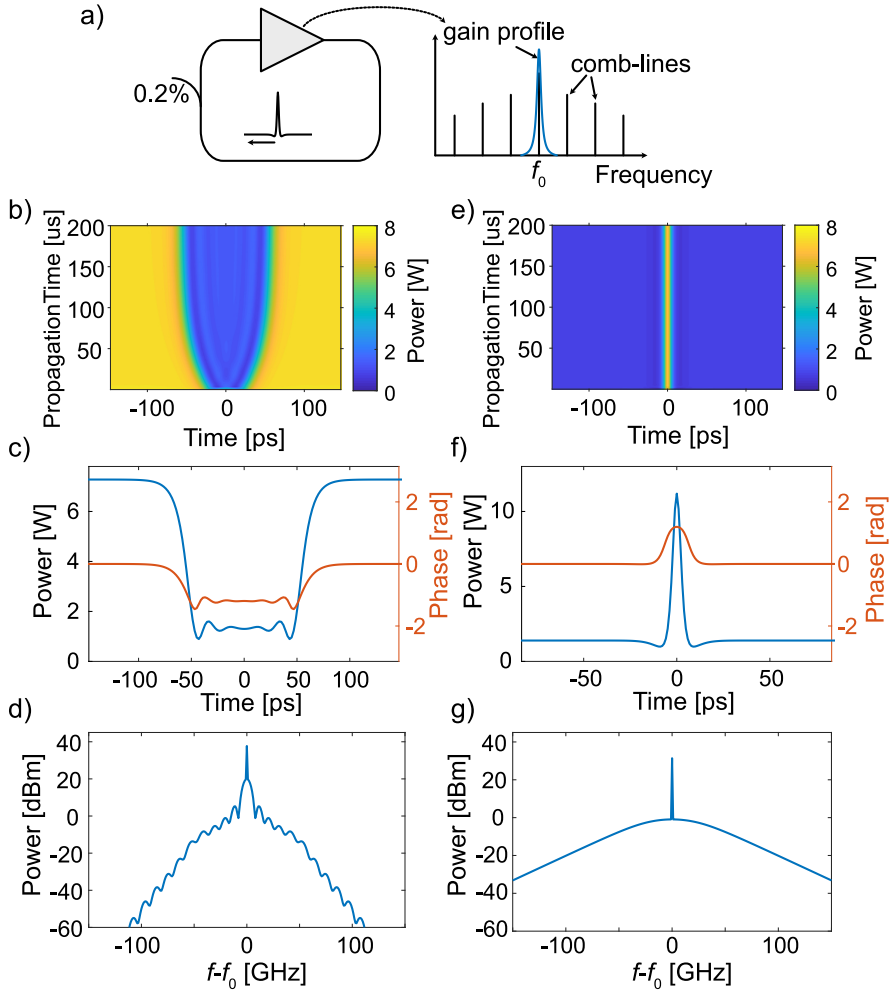


Figure 2.2: a) shows a layout of a laser cavity which can be used to generate a DKS. b) shows the evolution of a dark DKS from initiation, c) shows the temporal features and d) shows the spectrum. e) shows the evolution of a bright DKS from initiation, f) shows the temporal features and g) shows the spectrum.

Chapter 3

Microresonators and photonic molecules

Microresonators are small, typically sub-millimeter sized optical cavities. Much like other resonators, their operation is based on light recirculation which allows build-up of optical intensity at the resonant frequencies of the cavity. As such, they can be used in a variety of applications [99,100], including optical filters [101], sensors [102], modulators [103].

In this chapter, we will introduce the linear dynamics of microresonators, aiming at cavities that enable microcomb generation. While this study focuses on integrated microring resonators in silicon nitride, much of it will apply to optical resonators in general. In fact, much of the resonator physics had been described in Fabry-Perot cavities [104], and in fiber resonators [105,106], long before the realization of microresonators. The first section will cover the dynamics of one microring supporting a single waveguide mode, i.e. the dynamics that enable the DKSs in Paper A. The second section will introduce the dynamics of linearly coupled microresonators, often called photonic molecules, which were employed for generating a DKS in Papers C-F.

3.1 Characteristics of a single microring resonator

Typically, a microring resonator features a bus waveguide with a ring waveguide placed in close proximity (see Figure 3.1). The distance is short enough such that the evanescent field of the mode in both waveguides overlap, such that one mode induces a weak perturbation to the

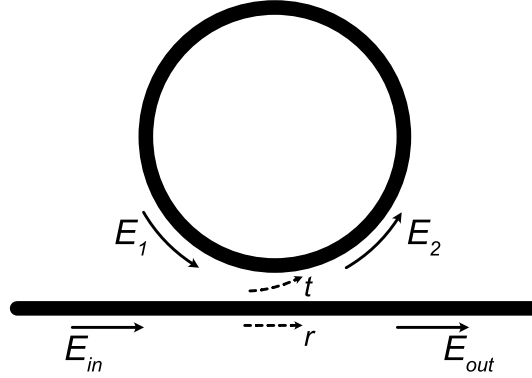


Figure 3.1: A basic layout of the microring resonator: A bus waveguide coupled to a ring waveguide.

other. This leads to periodic exchange of power between the two waveguides [107], where the coupling rate can be engineered by changing the distance between waveguides or the length of coupling interaction. Assuming weak coupling over a short distance of interaction, the coupling is approximated to occur in a single point [108] using the following coupling matrix:

$$\begin{bmatrix} E_{out} \\ E_2 \end{bmatrix} = \begin{bmatrix} r & it \\ it & r \end{bmatrix} \begin{bmatrix} E_{in} \\ E_1 \end{bmatrix}, \quad (3.1)$$

where t and r are real values representing the coupling coefficients relating the output optical field (E_{out}) to the input optical fields (E_{in}) and the optical fields in the cavity before and after the coupling regime (E_1 and E_2). The coupler is assumed to be lossless, such that $r^2 + t^2 = 1$. The fields E_1 and E_2 are also related by the optical propagation over a full roundtrip through the microring waveguide. Such propagation is described by equation 2.1 without the nonlinear effect:

$$\frac{\partial E}{\partial z} = -\frac{\alpha}{2}E + i\beta(\Delta\omega)E \quad (3.2)$$

where α is the intrinsic propagation loss, $\beta(\Delta\omega) = \beta_0 + \beta_1\Delta\omega + \beta_2/2(\Delta\omega)^2 + \dots$ is the frequency dependent propagation constant of the microring waveguide expanded around the reference frequency ω_{ref} , ω is the angular frequency and $\Delta\omega = \omega - \omega_{ref}$. The phase constant β_0 describes how the optical field accumulates phase at $\omega = \omega_{ref}$ as it

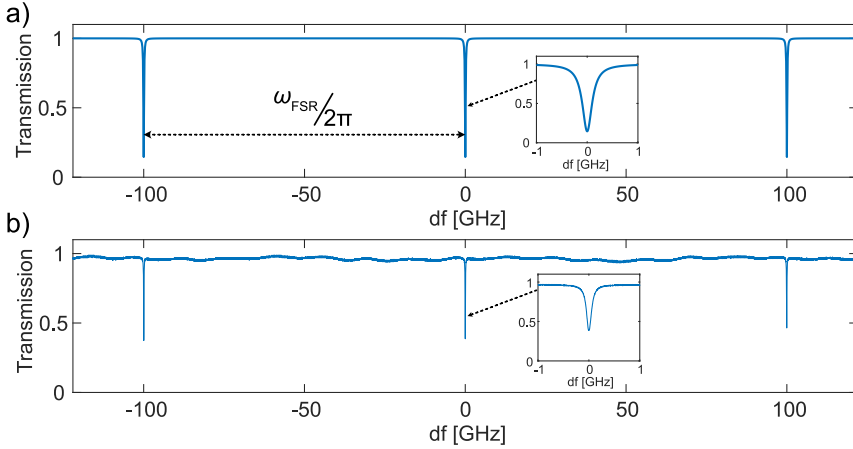


Figure 3.2: a) shows a microring transmission spectrum according to equation 3.4, using parameters $a = 0.9978$, $r = 0.995$, $\beta_0 = 0$, $\beta_1 = 6.67 \text{ ps/km}$, $\beta_2 = 1000 \text{ ps}^2/\text{km}$ and $L = 1.5 \text{ mm}$. The x-axis shows the offset frequency (df) with regards to the centered resonance. The inset shows a closer look at the center resonance. b) shows a measured spectrum of a microresonator with characteristics similar to those in a).

travels around the microring. Solving this equation, we relate the optical fields in the microring with

$$E_1 = E_2 e^{(-\alpha/2 + i\beta(\Delta\omega))L}, \quad (3.3)$$

where L is the roundtrip length of the microring.

The system of equations formed by equation 3.1 and equation 3.3 describes the linear response of the microring. Using these equations, the power transmission can be derived as [109, 110]

$$T(\Delta\omega) = \frac{|E_{out}(\Delta\omega)|^2}{|E_{in}(\Delta\omega)|^2} = \frac{a^2 - 2ra \cos(\beta(\Delta\omega)L) + r^2}{1 - 2ra \cos(\beta(\Delta\omega)L) + (ra)^2}, \quad (3.4)$$

where $a^2 = e^{-\alpha L}$ is the roundtrip attenuation of optical power. The equation describes the presence of resonances in the transmission spectrum located at the longitudinal modes of the cavity (see figure 3.2a). The resonance locations are defined by $\beta(\Delta\omega)L = 2\pi\mu$, where μ is the longitudinal mode number. The resonance separation, also called free spectral range (FSR), typically has a small spectral variation due to

GVD and higher order dispersion. The resonances can be characterized based on their width and depth, which are factors governed by the cavity losses.

Equation 3.4 is extremely useful for experimental characterization since the transmission is relatively easy to measure. This is typically done using a calibrated frequency-swept laser as an input optical field, while the output power is measured using a photodiode [111,112]. A plot of such a measurement is displayed in Figure 3.2b. The measurement shows how the resonance depth has a wavelength dependence. Thus, when characterizing the microcavity, we cannot apply equation 3.4 to all resonances at the same time. Rather, we consider each resonance individually.

In the next subsection, we will take a closer look at how cavity losses can be characterized from the width and depth of each resonance. The second subsection discusses the wavelength dependence of the propagation constant and how to characterize the dispersion of microcavities.

3.1.1 Cavity losses and Q factors

The transmission profile of a resonance is influenced by the cavity losses, both intrinsic losses (a) and coupling losses (r). The impact of the losses is seen in the full width at half maximum (ω_{FWHM}) and depth (described by R) of the resonance (see figure 3.3). For the purpose of analysing these characteristics, it is useful to approximate the cosine term of equation 3.4 with $\cos(x) \approx 1 - x^2/2$, which holds fairly well when cavity losses are low. The result is a Lorentzian shaped function

$$T = \frac{(\beta L)^2 + R(\Gamma/2)^2}{(\beta L)^2 + (\Gamma/2)^2}, \quad (3.5)$$

$$R = \frac{(r - a)^2}{(1 - ra)^2}, \quad \Gamma = 2\frac{(1 - ra)}{\sqrt{ra}} = 2\pi\frac{\omega_{FWHM}}{\omega_{FSR}} = \frac{2\pi}{\mathcal{F}}. \quad (3.6)$$

where \mathcal{F} is the finesse of the cavity, describing the sharpness of resonances with regards to FSR. With prior knowledge of the FSR, finding the FWHM and resonance depth is enough to determine the intrinsic and extrinsic loss parameter values, a and r . Figures 3.3a-c show resonance examples under the conditions of over coupling ($a > r$), under coupling ($a < r$) and critical coupling ($a = r$). The figures show that the resonance depth is impacted by the difference between a and r , where the critically coupled resonance completely shuts off the transmission.

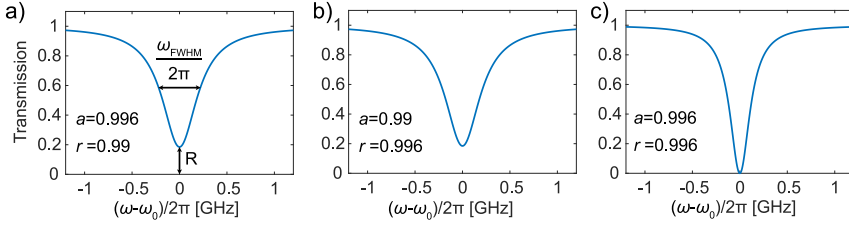


Figure 3.3: a) shows the transmission spectrum of a single resonance with overcoupled conditions $a > r$. The full width half maximum and resonance depth are indicated in the plot. b) shows a resonance with undercoupled conditions $a < r$. c) shows a resonance with critical coupling conditions $a = r$.

The FWHM increases as the overall losses increase. Thus, the FWHM in Figures 3.3a-b remains the same because they have the same overall roundtrip losses, while Figure 3.3c has a narrower resonance due to lower amount of total losses.

Note that a and r are tangled in the equations, such that it is not possible to tell from the transmission spectrum if the resonance is undercoupled or overcoupled, as displayed by Figures 3.3a-b. Only in the critically coupled case (see figure 3.3c) is this problem resolved, because $a = r$. To reliably resolve this issue, one needs to record both the phase and power response of resonance, which requires coherent detection [109, 112]. In practice, when there is a large difference between a and r , this can be resolved using prior knowledge of the design, which was the approach taken when characterizing the microrings in papers C-F.

The losses in resonator cavities are commonly represented by the quality factor (Q), which describes the number of optical cycles experienced by an optical field in the resonator cavity before the intrinsic and extrinsic losses reduce its energy by a factor $1/e$. It relates to extrinsic and intrinsic losses through

$$Q = \frac{\omega_0}{\omega_{FWHM}} = \frac{\omega_0 \mathcal{F}}{\omega_{FSR}} \approx \frac{\omega_0 n_g L \sqrt{ra}}{2(1-ra)c_0}, \quad (3.7)$$

where ω_0 is the frequency at center of resonance, n_g is the group index and c_0 is the speed of light in vacuum. The quality factor is often described as a combination between the extrinsic and intrinsic quality factors (Q_i and Q_e). Assuming low intrinsic and extrinsic losses, these can be approximated as

$$Q^{-1} \approx Q_i^{-1} + Q_e^{-1}, \quad (3.8)$$

$$Q_i = \frac{\omega_0 n_g L \sqrt{a}}{2(1-a)c_0}, \quad Q_e = \frac{\omega_0 n_g L \sqrt{r}}{2(1-r)c_0}. \quad (3.9)$$

The quality factor carries much significance when it comes to buildup of power in the microcavity. Such buildup of power is essential for microcombs, since they operate through the Kerr effect. The power buildup factor at center of resonance can be found as [110]

$$\frac{|E_1(\Delta\omega)|^2}{|E_{in}(\Delta\omega)|^2} = \frac{(1-r^2)a^2}{(1-ra)^2} \propto \frac{at^2 Q^2}{r}. \quad (3.10)$$

By approximating $t^2 \propto Q_e^{-1}$ and assuming that both intrinsic and extrinsic losses are low ($r, a \approx 1$) we get

$$\frac{|E_1(\Delta\omega)|^2}{|E_{in}(\Delta\omega)|^2} \propto \frac{Q^2}{Q_e}. \quad (3.11)$$

Thus, the quality factors limit the amount of buildup allowed in the microcavity. Since the coupling rate can be managed in design, realizing microcomb operation at low power levels will ultimately be limited by the intrinsic losses. For silicon nitride microresonators, these intrinsic losses are usually dominated by scattering due to sidewall roughness of the waveguides [113]. Reducing the impact of these losses [43], was an essential part of realizing the low-power microcombs in Papers D-F.

3.1.2 Dispersion in microresonators

Microcomb generation is sensitive to the location of resonances. In particular, the FSR and GVD affect important microcomb dynamics, such as the repetition rate and number of lines generated. Thus, it is important to design the length of the cavity and the cross-section of the microring waveguide to optimize these parameters, as is discussed in Paper A. After fabrication, the design can then be evaluated from the resonance distribution. Such distribution is defined by the propagation constant through

$$\beta(\omega - \omega_{ref}) = \beta_0 + \frac{\beta_1}{1!}(\omega - \omega_{ref}) + \frac{\beta_2}{2!}(\omega - \omega_{ref})^2 + \dots = 2\pi\mu/L, \quad (3.12)$$

where μ is an integer number describing the longitudinal mode number. The resonance frequencies ($\omega = \omega_\mu$) are found as solutions to this

equation for each integer value μ . The FSR can be calculated using $\omega_{FSR} = 1/\beta'(\omega - \omega_{ref})L$, where $\beta'(\omega - \omega_{ref})$ is the derivative of the propagation constant. As a simple approximation, the FSR can be assumed to be a fixed value $\omega_{FSR} = 1/\beta_1 L$. For higher accuracy we need to take the GVD and higher order dispersion into account, as they lead to spectral variations in the FSR (see figure 3.4).

The phase constant, β_0 , describes the acquired phase of the optical field per length at frequency ω_{ref} . The acquired phase over a whole roundtrip will be $\beta_0 L = n2\pi + \phi$, where n is an integer number and $\phi \cdot \omega_{FSR}/2\pi$ is the separation between ω_{ref} and ω_0 . It is common practice to set $\omega_{ref} = \omega_0$ when characterizing microcavities, which effectively sets $\beta_0 = 0$.

Equation 3.12 can be applied in a straightforward manner to characterize devices based on their experimentally measured transmission spectrum. The resonance frequency ω_μ is determined by finding the center of resonance (see figure 3.4a-b). We assign mode numbers to the resonances centered near our reference frequency ω_{ref} . The length of the cavity L is determined from the designed microring layout. The only missing parameters in equation 3.12 are the β parameters, which can be found through polynomial fitting.

It is worth noting that there exists another approach to define dispersion of microresonators which is commonly employed in the microcomb community [114, 115], which was used in Papers C-F. This approach maps the resonance locations according to

$$\omega_\mu = \omega_0 + D_1\mu + \frac{D_2}{2!}\mu^2 + \dots, \quad (3.13)$$

where $D_1/2\pi$ is the FSR of the cavity and $D_2/2\pi$ describes a linear change in FSR. We can relate these parameters to equation 3.12 with $D_1 = \frac{2\pi}{\beta_1 L}$ and $D_2 = -\frac{D_1^3 L}{2\pi}\beta_2$ [115]. The dispersion profile is often visualized using the integrated dispersion $D_{int} = \omega_\mu - \omega_0 - D_1\mu$. An example of such a visualization is given figure 3.4c, where normal GVD can be observed as a negative parabolic curvature.

The propagation constant is impacted by more factors than frequency and cavity length. The temperature of the resonator can also have a significant impact on the location of resonances. In silicon nitride microrings, such temperature dependence is mainly due to the thermo-optic effect [116–118], which causes the refractive index to linearly increase with temperature. As a consequence, the center frequency of the resonance spectrum shifts on the scale of $-1 \text{ GHz}/^\circ\text{C}$ and the FSR shifts

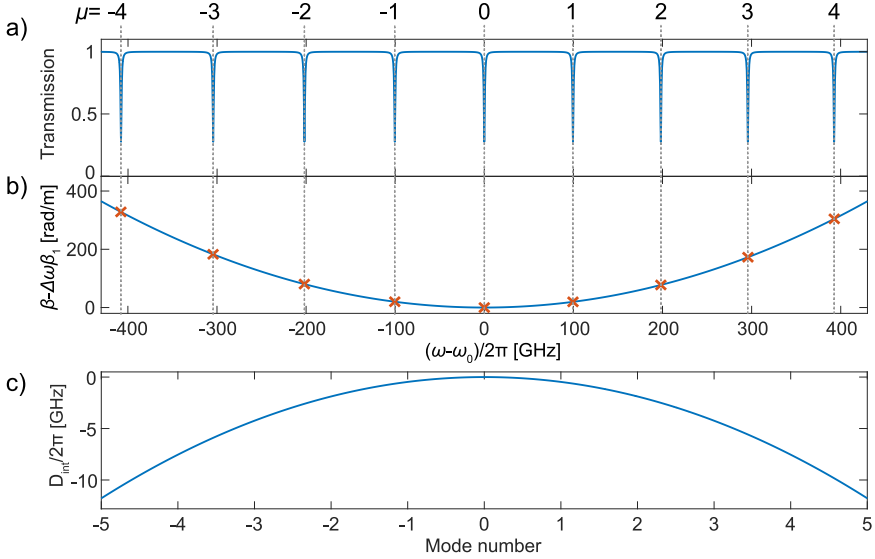


Figure 3.4: a) shows a microring transmission spectrum according to equation 3.4 with $\omega_{ref} = \omega_0$, and using parameters $a = 0.99$, $r = 0.968$, $\beta_0 = 0$, $\beta_1 = 6.67 \text{ ps/km}$, $\beta_2 = 100000 \text{ ps}^2/\text{km}$ and $L = 1.5 \text{ mm}$. The GVD causes the FSR to change with frequency, which means that the mode numbers are not appearing at equally spaced frequencies. The GVD is rather exaggerated for illustration purposes, such that this uneven separation becomes noticeable when displaying only a few resonances. b) shows the variation in propagation constant with frequency, with effects of β_1 and β_0 subtracted. It shows clearly the positive parabolic curve caused by the normal GVD term, but this curve becomes negative when anomalous dispersion is considered. The red markings correspond to the location of the resonances. c) shows the dispersion profile of the same cavity using the integrated dispersion.

changes on the scale of $-1 \text{ MHz}/^\circ\text{C}$ [119]. The benefit of such temperature dependence is that it allows tuning of the microcomb operation by placing a heater on the microcavity, which was an essential feature in Papers D-F. However, this also comes with a cost, since microresonators typically need to be thermally stabilized to avoid drifts in microcomb frequencies.

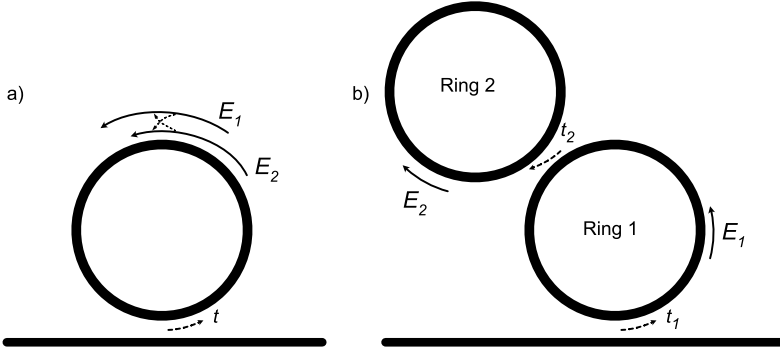


Figure 3.5: Two embodiments of photonic molecules using microrings, with a) showing linear coupling between two waveguide modes propagating in the same ring, and b) showing the interaction between two linearly coupled microrings, each with single-mode operation.

3.2 Linear dynamics of photonic molecules

Introducing linear coupling between resonant structures results in avoided mode-crossings — a splitting in the longitudinal modes of the cavities similar to split energy levels of diatomic molecules [21, 120]. Due to this analogy, coupled photonic cavities are often referred to as photonic molecules. Such structures allow dynamics and enhancements beyond that of a single resonator structure, enabling opportunities in several research fields such as microwave photonics [121], topological photonics [122, 123] and microcombs [124, 125].

Here, we discuss the linear dynamics of diatomic photonic molecules, focusing on microring structures for microcomb generation. There are a few different approaches to realize such linear coupling between modes. One approach is to employ a single physical resonator with coupling between waveguide modes (see figure 3.5a), where the modes can be either co-propagating or counter-propagating. While these waveguide modes are orthogonal in theory, they will often exhibit perturbations due to small discontinuities in the waveguide cross section, leading to linear coupling (κ) between the two modes [126, 127]. Such perturbations often appear due to sidewall roughness of the microring waveguide. This can introduce resonance-splits which are typically unwanted, since they can impede or distort the generation of soliton microcombs [115, 128].

However, there are other cases where the sidewall roughness induced mode-splitting has been of benefit. In [129], such mode-splitting enabled deterministic generation of a single DKS in the anomalous dispersion regime. Also, in normal dispersion waveguides, such a mode-split is essential for the generation of dark DKS from a CW laser as was shown in paper C.

The design in paper C had some practical weaknesses. One weakness is that the sidewall roughness is a parasitic effect that is hard to engineer in practice. This can be overcome by engineering variations in the ring waveguide, e.g. by using Bragg gratings in the ring structure [54]. A second weakness is that both waveguide modes share the same physical space, such that any changes to the refractive index of the waveguides will affect both modes in a similar manner. This means that it is extremely challenging to tune the dispersion of each resonant mode family separately.

Another approach for realizing photonic molecules is to use linearly coupled microrings (see figure 3.5b). Such structures offer more control over the design parameters, as the coupling between cavities can be easily controlled by changing the proximity of the two microrings. Furthermore, the thermal coupling between the two cavities is minimal, allowing the resonances of the two modes to be tuned separately via heaters on the two resonators [130]. This feature was essential for generating DKS microcombs in papers D-F.

In the following subsections, we will discuss the fundamental dynamics of linearly-coupled resonators.

3.2.1 Dispersion profile of photonic molecules

Let us consider two weakly coupled resonators using either design in figure 3.5. Instead of using the spatial dependence (as in equation 3.2), we consider a time dependence $e^{\zeta^{(1)}t}$ and $e^{\zeta^{(2)}t}$ for the two resonators, as it gives a more intuitive picture of the coupling dynamics. Such a system can be modelled by [107, 131]

$$\begin{aligned}\frac{\partial E_1}{\partial t} &= i\zeta^{(1)}E_1 + i\kappa E_2, \\ \frac{\partial E_2}{\partial t} &= i\kappa E_1 + i\zeta^{(2)}E_2,\end{aligned}\tag{3.14}$$

where κ is the coupling coefficient between modes in cavity 1 and 2, and $\zeta^{(a)} = i1/\tau_a + \omega^{(a)}$ with decay rate τ and frequency ω for mode a . The

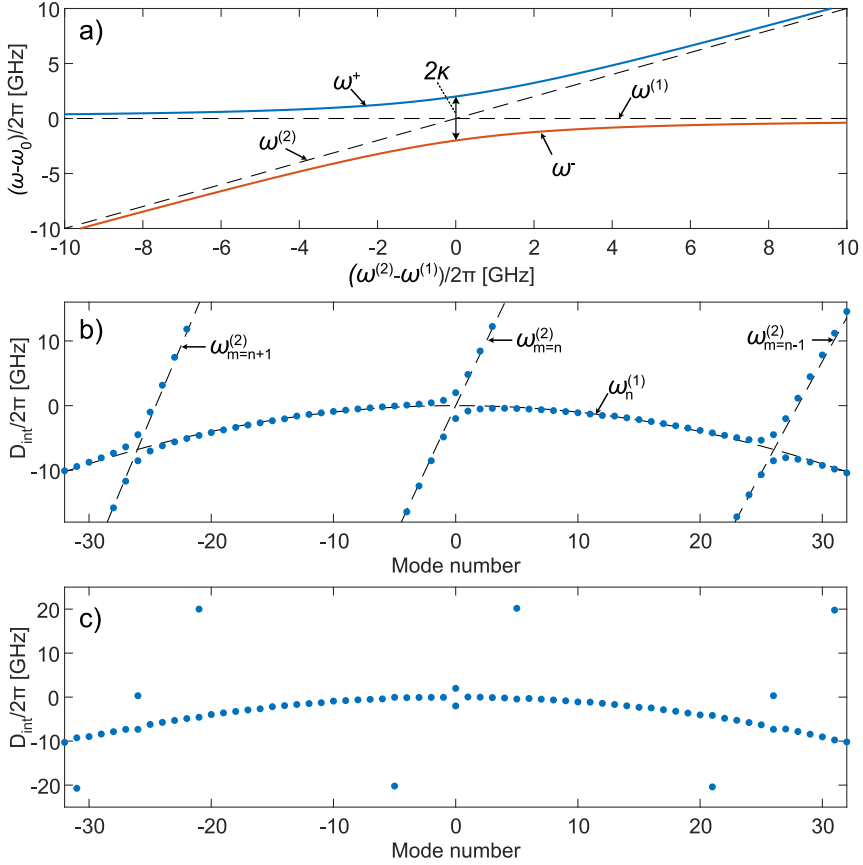


Figure 3.6: a) shows the interaction between resonances of linearly-coupled resonant cavities. The supermodes (ω^+ and ω^-), the uncoupled modes ($\omega^{(1)}$ and $\omega^{(2)}$) and the coupling factor κ are marked in the figure. b) shows the distribution of resonances (blue) of two linearly coupled cavities, using cavity 1 as a reference ($D_{int} = \omega - \omega_0 - D_1^{(1)}n$). The dashed lines show where the resonances would be located in absence of coupling. Periodic mode crossings appear due to the mismatch in FSR between $\omega^{(1)}$ and $\omega^{(2)}$. For each crossing we have the modes of $\omega_n^{(1)}$ interacting with $\omega_{n-1}^{(2)}$, $\omega_n^{(2)}$ and $\omega_{n+1}^{(2)}$ where indicated in the figure. c) the resonance separation of cavity 2 is changed so that it is roughly 5 times larger than that of cavity 1. This reduces the number of resonances experiencing frequency shifts in cavity 1.

coupling allows the resonant fields to exchange power, breaking the orthogonality between them. One of the consequences is that the resonant

frequencies of E_1 and E_2 will not be defined by $\zeta^{(1)}$ and $\zeta^{(2)}$ independently. To determine the resonant frequencies, a new basis is found for the perturbed system with orthogonal modes named supermodes. These supermodes define the locations of the resonances of the coupled system, written as a superposition of the orthogonal modes of the unperturbed system. The resonance locations of the supermodes can be derived from equation 3.14 as [107]

$$\zeta_{\pm} = \frac{\zeta^{(1)} + \zeta^{(2)}}{2} \pm \sqrt{\left(\frac{\zeta^{(1)} - \zeta^{(2)}}{2}\right)^2 + |\kappa|^2}, \quad (3.15)$$

with an example displayed in figure 3.6a. The losses will have negligible impact on the resonance locations and are thus not included in the example, hence ζ is replaced by ω . The uncoupled ($\kappa = 0$) resonance locations in each resonator is labelled with $\omega^{(1,2)}$. We tune the location of $\omega^{(2)}$ to modify the distance between the two resonances. In the uncoupled case, the resonances are unaffected by each other's proximity, as is indicated by the dashed lines. When the coupling is turned on ($\kappa = 2GHZ$) we see that the supermodes are shifted compared to the uncoupled case. However, the shift is only significant when the difference between resonant frequencies ($|\omega^{(1)} - \omega^{(2)}|$) is not much larger than the coupling rate (κ). Note that even though the uncoupled modes 1 and 2 cross, the supermodes avoid each other at the crossing. It is for this reason that they are often referred to as an avoided mode-crossing. At $\omega^{(1)} = \omega^{(2)}$, we reach the minimum distance between resonances, $\omega^+ - \omega^- = 2\kappa$. This fact is extremely useful when experimentally estimating the linear coupling between microrings in Paper D. Using the microring heaters, the coupling rate was measured by tuning the resonances of the two microrings until minimum frequency separation was reached.

Let us now investigate how equation 3.15 impacts the dispersion profile of linearly-coupled resonators. For this we consider resonance distribution $\omega_n^{(1)}$ and $\omega_m^{(2)}$, where n and m are the longitudinal-mode numbers of resonators 1 and 2. The resonances are distributed with a normal GVD using equation 3.13, with parameters $\omega_0^{(1)} = \omega_0^{(2)}$, $D_1^{(1)}/2\pi = 100GHZ$, $D_1^{(2)}/2\pi = 104GHZ$, $D_2^{(1)}/2\pi = D_2^{(2)}/2\pi = -20MHZ$, and $\kappa = 2GHZ$. The resonance locations of the coupled system are plotted as an integrated dispersion profile in figure 3.6b. The dashed lines show the dispersion of the resonators in absence of coupling, revealing the negative curvature of $\omega_n^{(1)}$ due to normal GVD. The resonances of the coupled

system form not only one, but multiple mode crossings in an evenly spaced pattern. This is due to the walk-off in FSR between the two resonator modes, where the mode separation between mode crossings is approximately $D_1^{(1)}/(D_1^{(1)} - D_1^{(2)})$. This FSR walk-off can be easily engineered in coupled microrings by changing length mismatch of the microrings. Looking closely at each mode crossing, we see that resonances are shifted significantly from the uncoupled case, forming the supermode pattern discussed in figure 3.6a. This shifting of the cavity resonances was essential for realizing the phase-matching required for DKS initiation in the normal dispersion regime in Papers C-E.

In figure 3.6c, we again consider the same coupled resonators, but with a drastically larger FSR in cavity 2 ($D_1^{(2)}/2\pi = 520 \text{ GHz}$). As a result, only one in every 5 resonances in resonator 1 experience a significant shift due to coupling. This approach is extremely useful to realize a shift in one resonance of a cavity without affecting the others, as was the case in paper F.

3.2.2 Transmission response of photonic molecules

Having discussed the distribution of photonic molecule resonances, we now investigate how the spectral power response of such devices may look like. For this, we apply the rate equations from perspective of the propagation constant (β), which was used to solve the propagation of linearly coupled waveguide modes in Paper C. The rate equations are written as

$$\begin{aligned}\frac{\partial E_1}{\partial z} &= i\rho_1 E_1 + i\kappa_z E_2, \\ \frac{\partial E_2}{\partial z} &= i\kappa_z E_1 + i\rho_2 E_2,\end{aligned}\tag{3.16}$$

where $\rho_n = i\alpha_n + \beta^{(n)}$ and κ_z is the coupling rate over distance between cavities. According to our simulations, this coupling rate can be approximately linked to the temporal coupling rate from equation 3.14 as $\kappa_z \approx \kappa \cdot 2\pi(L^2 D_1^{(1)} D_1^{(2)})^{-1/2}$. The propagation constants of the supermodes are found as

$$\rho_{\pm} = \frac{\rho_1 + \rho_2}{2} \pm \sqrt{\left(\frac{\rho_1 - \rho_2}{2}\right)^2 + |\kappa_z|^2}.\tag{3.17}$$

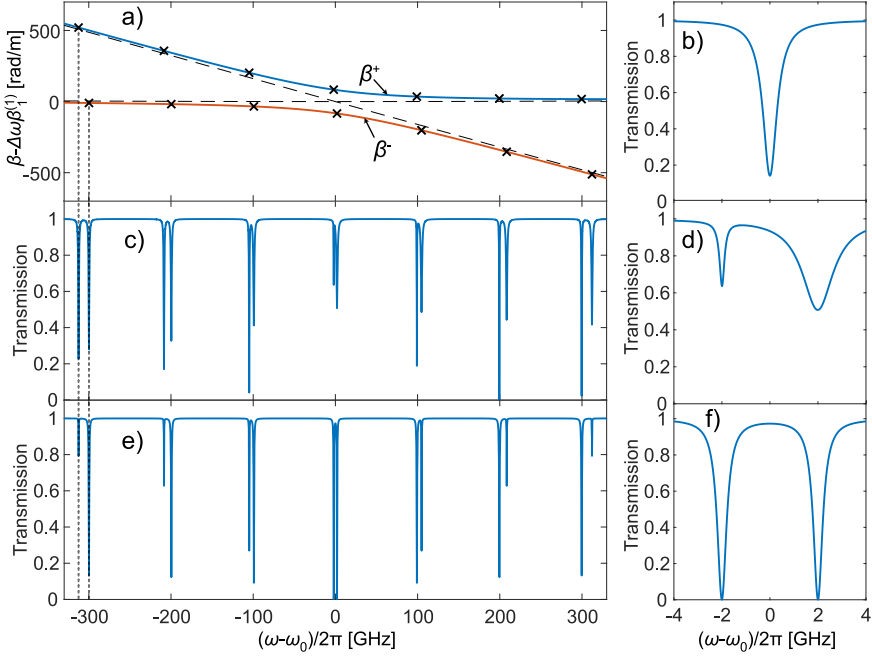


Figure 3.7: a) shows the coupled-mode dispersion profile of the same system as figure 3.6b, using the formalism of equation 3.17. b) shows a resonance profile of cavity 1 with $\kappa = 0$. c) is a resonance transmission with power coupled from the bus waveguide into both waveguide modes ($\theta_1 = 0.03$, $\theta_2 = 0.05$) and with $\kappa/2\pi = 2\text{GHz}$. The shaded lines connect the resonances to the dispersion profile in a), indicating to which mode they belong. The resonances of the two modes are shown to shift across one another due to the difference in group velocity. d) shows a zoom-in to the center of the resonance transmission in c). In contrast to the uncoupled resonance in b), the mode-coupling causes the resonances to shift off center and change in extinction ratio. Finally, e) and f) show a similar response as c) and d), with $\theta_2 = 0$. The effect is that the resonances corresponding to mode 2, seen in a) as the diagonal uncoupled mode, will disappear when located far away from resonances of mode 1

Let us assume negligible losses such that $\rho \approx \beta$. The location of these resonances will not be defined by the uncoupled modes, but rather the supermodes as $\beta^+L = 2\pi n$ and $\beta^-L = 2\pi m$, where n and m are integer numbers. An example of the distribution of the resonances is shown in figure 3.7a, using the same dispersion and coupling configuration as figure 3.6b. The model successfully predicts the presence of supermodes

with resonances appearing in the same location as in figure 3.6b.

We now study the transmission response of these resonances assuming a system with two linearly coupled waveguide modes in a single microring. Such systems can allow direct coupling from the bus waveguide to either waveguide mode, as was the case in Paper C. The transmission response of these resonances can be modeled using a system combining equation 3.14 with a coupling matrix describing a directional coupler between the bus waveguide and the two modes of the microcavity, with the model detailed in Paper C. This system is numerically solved to display a transmission spectrum of the microcavity in figure 3.7. The dispersion parameters and coupling are the same as in figure 3.7a, with $\alpha_1 = \alpha_2 = 9.2 \text{ m}^{-1}$ and the power coupling ratio to mode 1 and 2 is $\theta_1 = 0.03$ and $\theta_2 = 0.05$. In absence of coupling, both modes $\beta^{(1)}$ and $\beta^{(2)}$ are centered at ω_0 , with a resonance of $\beta^{(1)}$ displayed in figure 3.7b. Turning on the coupling between modes results in the transmission spectrum is displayed in 3.7 c-d. It shows resonances whose locations are described by the dispersion profile in figure 3.7a. Far away from the mode crossing, the resonances of the cavities are not impacted by the mode coupling. These can be used to characterize the cavities separately using the single-mode model from section 3.1 to retrieve the dispersion and losses. However, moving closer to the center of the mode-crossing, we see that the extinction ratio and shape of the resonances starts to change, which is evident when comparing figure 3.7d to figure 3.7b. Thus, it is challenging to use the shifted resonances to characterize each cavity individually. However, the mode-crossing is useful for identifying the coupling coefficient, e.g. through fitting of the resonance distribution near the avoided mode crossing with equation 3.14. Alternatively, in the special case when $\beta^{(1)} = \beta^{(2)}$ as is the case for the resonances displayed in figure 3.7 d, the resonance difference can be used to determine the coupling coefficient.

Another interesting case is presented in figure 3.7e-f, where the coupling between bus waveguide and mode 2 has been turned off ($\theta_2 = 0$). This describes the coupled microring system in paper D, where cavity 1 is the main ring and cavity 2 is the auxiliary ring. In this case, the resonances of cavity 2 only appear when coupled with the resonances of cavity 1. An intuitive explanation of this phenomenon is that with $\theta_2 = 0$, cavity 2 is reliant on cavity 1 to supply power. Therefore, in places where cavity 1 is not resonant, no power can be coupled to cavity 2. This effect made the dispersion profile of cavity 2 challenging to deter-

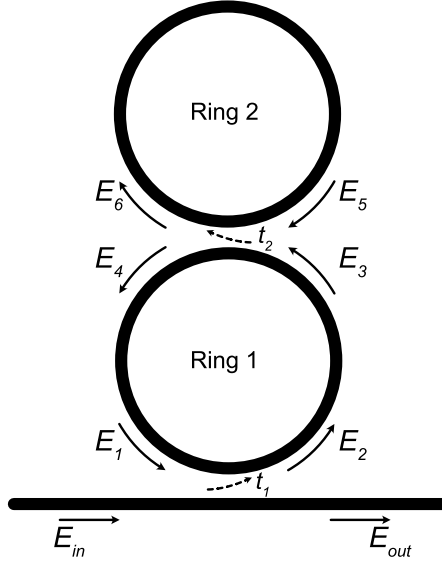


Figure 3.8: A basic layout of two linearly coupled microrings

mine in paper D, where only the FSR was estimated. A simple solution to this problem is to include a second bus waveguide which is weakly coupled to cavity 2. This allows the second microring to be directly characterized.

A system with two linearly-coupled microrings can also be modelled using a point coupling scheme instead of a rate equation. Such a scheme was used for the simulations in Papers D-F. The coupling regimes of the two coupled rings can be approximated with matrices:

$$\begin{bmatrix} E_{out} \\ E_2 \end{bmatrix} = \begin{bmatrix} r_1 & it_1 \\ it_1 & r_1 \end{bmatrix} \begin{bmatrix} E_{in} \\ E_1 \end{bmatrix}, \quad (3.18)$$

$$\begin{bmatrix} E_6 \\ E_4 \end{bmatrix} = \begin{bmatrix} r_2 & it_2 \\ it_2 & r_2 \end{bmatrix} \begin{bmatrix} E_5 \\ E_3 \end{bmatrix}, \quad (3.19)$$

where the input and output fields are depicted in figure 3.8.

For the next step, we make the assumption that the two rings have the same physical length. This is a somewhat crude approximation, since the FSR difference between the two cavities is typically achieved by changing the cavity length. However, by modifying the group index instead, we can manipulate the optical propagation length to catch the FSR difference of

the cavities. Using this approximation requires the propagation constant of the cavity to be adjusted accordingly to project the correct dispersion and losses per roundtrip. For the microcomb generation in papers D-F, this approximation was acceptable, since small variations in GVD or propagation losses of the auxiliary cavity did not have significant impact on the simulated microcomb dynamics.

The propagation in the microrings is derived in a manner similar to equation 3.3.

$$\frac{\partial E_n}{\partial z} = -\frac{\alpha_n}{2} E_n + i\beta^{(n)}(\Delta\omega)E_n, \quad (3.20)$$

where n stands for the mode in ring n . Using a procedure similar to [132], the transmission can be derived as

$$T = \frac{E_{out}}{E_{in}} = \frac{r_1 - K a_1 e^{i\beta^{(1)}L}}{1 - K r_1 a_1 e^{i\beta^{(1)}L}}, \quad (3.21)$$

$$K = \frac{r_2 - a_2 e^{i\beta^{(2)}L}}{1 - r_2 a_2 e^{i\beta^{(2)}L}}, \quad (3.22)$$

where $a_n = e^{-\alpha_n L/2}$. This model was used with the same parameters as presented in figure 3.7e, with the same overall coupling between modes per roundtrip. The resulting transmission spectrum is virtually identical to figure 3.7e, suggesting that this point-coupling model can be used interchangeably with equation 3.17. However, we expect such interchangeability only to be valid when the coupling rate is small, i.e. when mean-field approximations can be applied.

Chapter 4

Soliton generation in microresonators

Adding Kerr nonlinearity to the microresonator dynamics introduces a range of optical effects not available in the linear regime. Other than microcomb generation, this includes dynamics such as resonance shifts due to SPM and XPM which can be employed in all-optical logic gates [133,134] and third harmonic generation which can be employed for CW generation at new wavelengths [135,136] and in 2f-3f self-referencing [137]. Here we give a brief introduction to some of the Kerr nonlinear effects found in microresonators, with special focus on DKSs. The first section covers nonlinear dynamics in a single-mode cavity. The second section is about DKS generation in microresonators.

4.1 Nonlinear dynamics in a single cavity

The modeling of the Kerr nonlinear operation in a single-mode microresonator can be described in two parts: A nonlinear propagation over a full roundtrip and a coupling regime exchanging optical power between bus waveguide and ring. This system of equations is known in some fields as the Ikeda map [138,139]. These equations include a modified NLSE and the coupling matrix from equation 3.1

$$\begin{bmatrix} A_{out} \\ A_2 \end{bmatrix} = \begin{bmatrix} r & i\rho \\ i\rho & r \end{bmatrix} \begin{bmatrix} A_{in} \\ A_1 \end{bmatrix}, \quad (4.1)$$

$$\frac{\partial A}{\partial z} = i\gamma|A|^2A - \frac{\alpha}{2}A + i\beta_0A - \frac{i\beta_2}{2}\frac{\partial^2 A}{\partial t^2}. \quad (4.2)$$

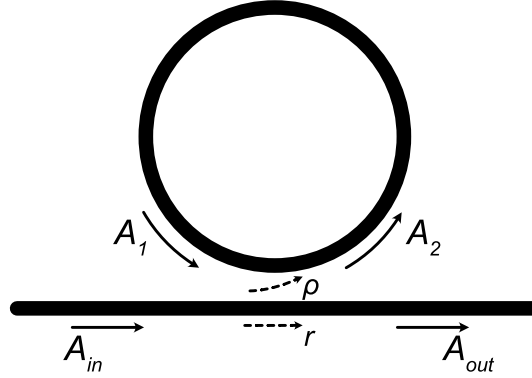


Figure 4.1: A basic layout of the microring resonator: a bus waveguide coupled to a ring waveguide.

The phase constant, β_0 , describes how the pump frequency accumulates phase as it circulates the cavity. Over a full roundtrip it effectively causes a constant phase offset, $\delta_0 = 2\pi\mu - \beta_0 L$, which is often called the detuning parameter. Note, that this constant phase shift is applied to all frequency components of A , while the phase of A_{in} is kept constant. The coupling between bus waveguide and ring is often presented in terms of power as $\theta = \rho^2$.

Defining the internal field (A) in a time window spanning the duration of a cavity roundtrip, a full roundtrip of the intracavity field can be easily simulated. This is done by first applying the coupling equation and then simulating propagation through the full length of the ring by solving equation 4.2 with the split-step method. Realistically, such a field will include noise due to the quantized nature of light, which can be included in the simulation by adding a photon with a random phase into each spectral bin onto the laser [140, 141].

4.1.1 The Lugiato-Lefever equation

The Ikeda map can be approximated as a single equation, which is sometimes called the Lugiato-Lefever equation (LLE). As such, it provides an extremely useful tool for mathematical analysis of Kerr nonlinear microcavities with DKS dynamics. It is named after the authors who first derived it to describe the optical spatial field in a nonlinear cavity [142], but it was later shown that it also applies for temporal fields [143].

To derive the LLE, the intracavity field is assumed not to change significantly over the span of a single roundtrip, a condition that is typically valid when considering high Q factors and low amount of phase shifts experienced by the optical field per roundtrip [143]. As such, the nonlinear propagation through the length of the cavity (L) can be approximated by

$$A_1^{(n)} = A_2^{(n-1)} + L \frac{\partial A_1^{(n)}}{\partial z}, \quad (4.3)$$

where n presents the number of roundtrips. The coupling regime gives

$$A_2^{(n-1)} = A_1^{(n-1)}(1 - \theta/2) + i\sqrt{\theta}A_{in}, \quad (4.4)$$

where, assuming that the coupling rate is low, the approximation $\sqrt{1 - \theta} \approx 1 - \theta/2$ has been applied. Combining equations 4.3 and 4.4, and substituting 4.2 leads to the LLE equation:

$$\frac{\partial A}{\partial \tau} = \frac{A^{(n)} - A^{(n-1)}}{t_R} = \frac{1}{t_R} \left[(-\sigma - i\delta_0 - L \frac{i\beta_2}{2} \frac{\partial^2}{\partial t^2} + iL\gamma|A|^2)A + i\sqrt{\theta}A_{in} \right], \quad (4.5)$$

where $\sigma = \frac{\theta + \alpha L}{2}$ and t_R is the roundtrip time, and τ is the slow time. This equation is often normalized [144], as was done in Paper F. The LLE has been widely used to investigate the dynamics of nonlinear cavities, such as bistability [143, 145], existence regimes of waveforms [145–147], modulational instability [140, 148] and dissipative Kerr solitons [27, 58, 149].

4.1.2 Bistability

The LLE can be used to describe a CW intracavity field of the cavity in presence of the nonlinear phase shift [143]. Assuming steady-state, the LLE is reduced to

$$i\sqrt{\theta}A_{in} = (\sigma + i\delta_0 - i\gamma L|A|^2)A. \quad (4.6)$$

Multiplying each side of the equation with its conjugate results in [144]

$$\theta|A_{in}|^2 = (\sigma^2 + \delta_0^2 + \gamma^2 L^2 P^2 - 2\delta_0 \gamma L P)P, \quad (4.7)$$

where $P = |A|^2$ is the intracavity power. This describes a third order polynomial in terms of P , which can be easily solved numerically. Then, by taking the angle of 4.6, the angle of the intracavity field is found as

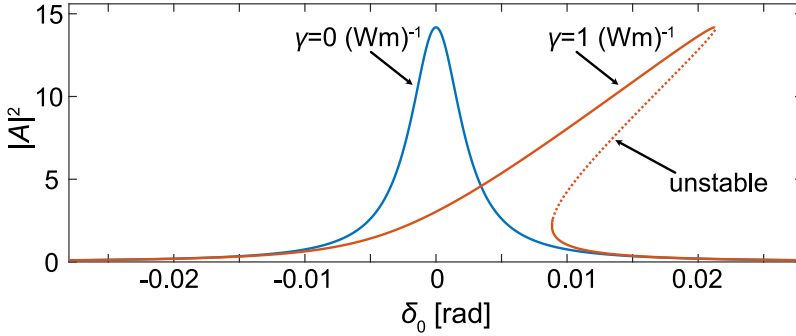


Figure 4.2: Solutions for the intracavity power assuming CW steady-state, with blue and red show the contrast between linear and nonlinear regime. The parameters were set as $P_{in} = 20 \text{ mW}$, $\sigma = 0.0024$, $\theta = 0.004$ and $L = 1.5 \text{ mm}$.

$$\angle A = \angle(iA_{in}) - \angle(\sigma + i\delta_0 - i\gamma L|A|^2). \quad (4.8)$$

The power levels of the CW steady-state solutions of a resonant cavity are plotted in figure 4.2. It shows how the resonances of the cavity become 'tilted' in the presence of a nonlinear phase shift. This leads to three possible solutions for the intracavity field, with one of them being unstable in presence of small perturbations [146]. These solutions were used to define the CW background when initiating DKSs in Papers A-B.

4.1.3 Modulational instability

The bistability analysis above only considered CW solutions. However, in the presence of small perturbations (e.g. noise), the microcavity can exhibit modulational instability (MI). This occurs when the CW field of power P provides parametric amplification to other frequency components which outweighs the cavity losses. As a result, new frequency components can be generated in the resonances of the cavity. Degenerate FWM leads to the parametric oscillations [23, 24, 150], with two or more comb lines being generated. The spacing of the generated comb-lines can be equidistant due to cascaded FWM, forming oscillating waveforms commonly named Turing rolls [146, 151], which are displayed in figure 4.3. These waveforms typically have a very low number of lines generated, much lower than typical DKSs. Thus, they are more suitable for applications that are not reliant on spectral coverage, such as efficient

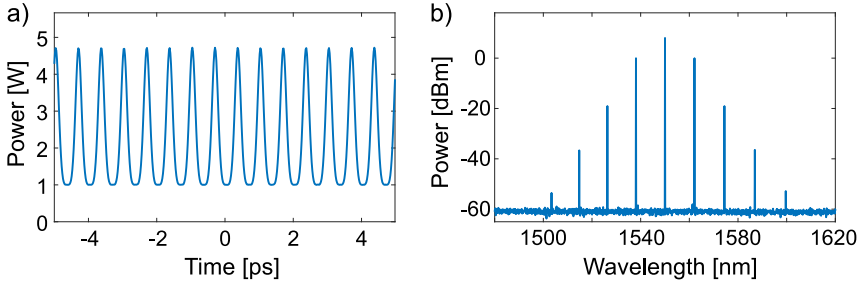


Figure 4.3: a) shows the temporal features of Turing rolls, with b) showing the corresponding spectrum. Parameters used were $\theta = 0.005$, $\beta_2 = -100 \text{ ps}^2/\text{km}$, $L = 1.5 \text{ mm}$, $FSR = 100 \text{ GHz}$, $\alpha = 0.5 \text{ m}^{-1}$, $\gamma = 1 \text{ (Wm)}^{-1}$, $\delta_0 = 0$, $P_{in} = 10 \text{ mW}$.

generation of CW lasers at new frequencies [152, 153] and generation of oscillations in the microwave or THz regime [154].

The presence of MI and Turing rolls are an essential part of DKS initiation when pumping with a CW laser. With adequate CW power, such DKS initiation can be achieved in anomalous GVD microrings by tuning the CW laser into resonance from the blue side towards the red [29, 155]. This is enabled by the fact that the existence regimes of Turing rolls and bright DKS are linked, either directly or through an intermediate chaotic regime [146, 156]. Figure 4.4a-b shows the evolution of the intracavity temporal field during such DKS initiation. As the detuning of the laser increases (i.e. the frequency is shifted towards the red) the intracavity power builds up, eventually leading to MI which generates Turing rolls and then chaotic states. At a certain detuning, where the CW steady-state resolves into bistability, the chaos subsides, with multiple bright DKSs appearing as shown in figure 4.4c-d. The presence of MI near the existence regime of DKSs is thus essential for initiation from a CW laser.

DKS initiation in the normal GVD regime also requires MI. However, due to the lack of phase matching in single-mode waveguides, MI will be extremely hard to achieve. The phase-matching condition for MI, assuming negligible higher-order dispersion, can be derived from the LLE as [140]

$$\Delta\Omega_m^2 = 2 \frac{\delta_0 - 2\gamma LP}{\beta_2 L}, \quad (4.9)$$

where $\Delta\Omega_m$ signifies the offset between CW pump and the frequency

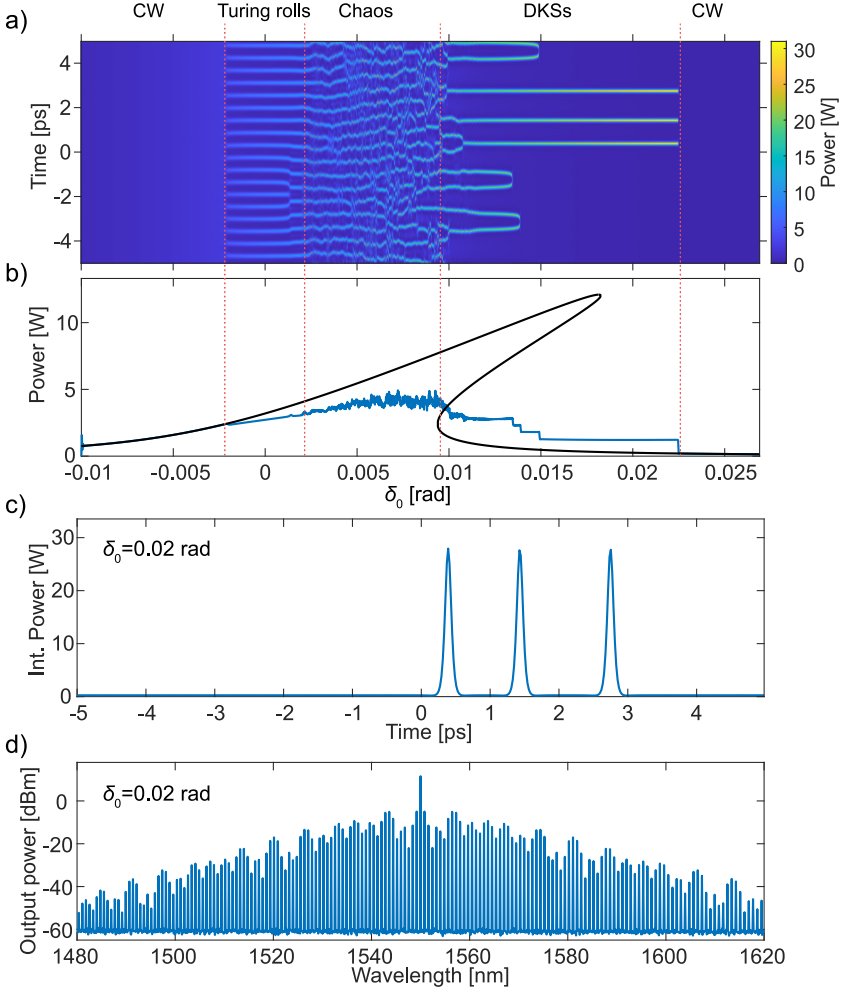


Figure 4.4: a) shows the evolution of the temporal field in an anomalous microring as the detuning is linearly scanned. It shows the generation of Turing patterns at $\delta_0 = 0$, chaos at $\delta_0 = 0.005$ rad and solitons appearing after $\delta_0 = 0.01$ rad. b) shows the corresponding evolution of the averaged intracavity power (blue) and the CW steady-state solutions. c) shows the temporal field at $\delta_0 = 0.02$ rad, with d) showing the corresponding spectrum. Parameters used were $\theta = 0.005$, $\beta_2 = -100$ ps²/km, $L = 1.5$ mm, $FSR = 100$ GHz, $\alpha = 0.5$ m⁻¹, $\gamma = 1$ (Wm)⁻¹, $P_{in} = 20$ mW.

where phase matching occurs. Note that the numerator ($\delta_0 - 2\gamma LP$) sets a limitation to the sign of the GVD. MI is accessible in the anomalous GVD regime when ($\delta_0 < 2\gamma LP$), which only requires $\delta_0 = 0$ to be fulfilled. However, in the normal dispersion regime, the requirement is ($\delta_0 > 2\gamma LP$), where Turing rolls can only be found using excessive pump power and high detuning [146]. Furthermore, the existence regime of normal DKSs and MI are not linked, since normal DKSs exist in the regime where ($\delta_0 < 2\gamma LP$). Normal DKSs are thus virtually impossible to initiate in single-mode normal GVD microrings when pumping with a CW laser.

One way of achieving phase matching in normal GVD waveguides is to introduce a mechanism which shifts the resonances of the cavity, affecting the detuning factor and the GVD profile of the cavity. Note that in this case the detuning factor should be determined by the offset from the CW pumped resonance, rather we use the 'comb detuning' introduced in Paper F. Such shifts can be accomplished using linearly coupled cavities [31, 52, 53, 157, 158], as was discussed in section 3.2. This was a key factor in Paper C-E, where such mode-coupling eased the phase-matching condition, allowing a DKS to be generated from MI. Other systems and dynamics can also enable DKS initiation in the normal GVD regime, such as second harmonic generation [159] and self injection-locking [55, 160]. We will revisit the topic of normal dispersion CW initiation in section 5.3.

Phase matching is not the only condition for MI. A second condition requires the intracavity power to rise beyond the gain threshold of the parametric oscillations [24, 161]. This intracavity threshold is defined by $P_{th} = \sigma/(\gamma L)$. Assuming critical coupling, this sets a threshold input power described by [140]

$$P_{in,th} = \frac{1}{\gamma L} (\sigma^2 + (\delta_0 - \sigma)^2), \quad (4.10)$$

where $\sigma = \frac{\theta + \alpha L}{2} \approx \frac{\omega_0 n_g L}{2c_0 Q}$. This sets a $1/Q^2$ dependence for the input power to achieve MI, underlining once again the importance of minimizing the losses of the cavity to realize low power operation. Thus, demonstrations of low-power operation of microcombs depend on realizing microcavities with high quality-factors [46, 47]. Indeed, high quality-factors were one of the key factors in Paper D and Paper F to realize microcomb generated with laser power of 5 mW or lower. Note however that the threshold also depends on the nonlinear parameter γ , which means that

the intrinsic Q requirements are somewhat relaxed in the case of highly nonlinear materials. For example, the microcombs generated with the one of the lowest threshold power achieved to date involved AlGaAs microresonators with mediocre Q-factors combined with an exceptionally high nonlinear index [57].

4.2 DKS generation in microresonators

The Ikeda map and LLE can support a DKS as a double balance of GVD with SPM and cavity losses with parametric amplification. Such a state was theoretically described in an anomalous cavity as early as the 90's [27, 145]. However, it was not until 2010 that this waveform was first experimentally demonstrated in an anomalous nonlinear fiber cavity [28] and in microresonators a few years later [29]. The anomalous DKS is essentially a bright pulse which sits on top of a CW background defined by the lower level of the CW bistability (see figure 4.5). The spectrum has a smooth envelope, with a line separation equal to the rate at which the DKS circulates the cavity. Both the temporal and spectral amplitudes of the bright DKS can be derived as a hyperbolic secant from the LLE [29, 58, 144]. Such studies have shown that solitons can only exist with the CW laser far red-detuned from resonance center, as is indicated by the figure 4.4. Due to the amount of CW power bypassing the cavity, this leads to a fundamentally limited conversion efficiency (the output power of the generated frequencies excluding the pump divided by the input CW power [59]) which can cause a lack of power in the generated comb lines. This was the main inspiration for Paper F, where the hindrance in conversion efficiency was mitigated by shifting the pumped resonance towards the red-side, allowing the pump to operate near center of resonance while the comb lines experience high red-detuning. Other methods to improve conversion efficiency have been demonstrated, such as microresonator nesting in laser cavities [62], pulsed pumping [60] and normal GVD DKSs [31].

The anomalous DKS can be initiated through MI using a CW laser by scanning the CW laser frequency across resonance from the blue side towards the red, as was shown in figure 4.4. Typically such initiation does not deterministically result in a single DKS. It is more likely, as indicated by figure 4.4c, that multiple DKSs (multi-DKS) are generated. The conversion efficiency of such multi-DKS states increases with the number of DKSs circulating the cavity. The resulting spectrum (see figure 4.4d) is

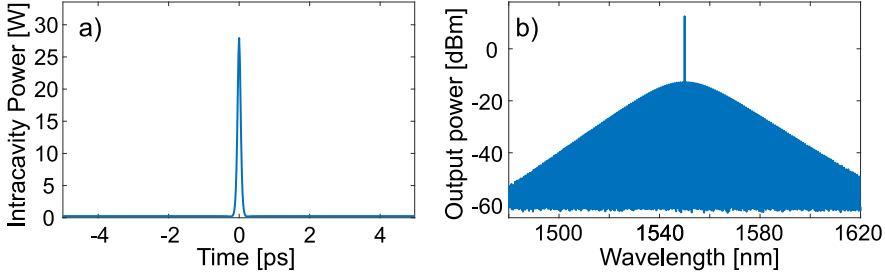


Figure 4.5: a) shows the temporal features of an anomalous DKS, with b) showing the corresponding spectrum. Parameters used were $\theta = 0.005$, $\beta_2 = -100 \text{ ps}^2/\text{km}$, $L = 1.5 \text{ mm}$, $FSR = 100 \text{ GHz}$, $\alpha = 0.5 \text{ m}^{-1}$, $\gamma = 1 \text{ (Wm)}^{-1}$, $\delta_0 = 0.02$, $P_{in} = 20 \text{ mW}$.

rather uneven which is typically undesirable for applications that require flatter distribution such as astrocombs [8] and optical telecommunication [Paper B]. Many approaches have been implemented to deterministically achieve a single DKS, such as employing the thermal phase shift [51] or interaction with a higher-order spatial mode [129].

The results of Papers E-F were interesting in the context of DKS initiation, as bi-directional initiation was possible, i.e. scanning the laser into resonance from either the blue side or the red side. Such dynamics are not available in a single-mode microresonators without added effects, such as the photorefractive effect [41] or interaction with a CW laser cavity [162]

DKS states can also be maintained in a single-mode normal-GVD microresonator. The temporal waveform of such normal DKSs are rather different from the anomalous DKS, forming a dark pulse on a CW background with oscillations at the bottom that decay towards the middle (see figure 4.6) [31, 163]. These waveforms are sometimes named platicons due to the high-power CW background [164]. The CW background and the bottom ripples are closely related to the CW steady-state solution of the bistability, where the normal DKS appears to switch between these two states. As such, it has been described as two switching waves, which move towards each other until their oscillatory tails lock together [98, 165]. A peculiar result of this is that the resulting pulse can exist in different states depending on how these oscillatory tails lock together, with each state having varying widths and a different number of ripples at the bottom of the pulse [147]. Switching between these states

was observed in Paper C as a change in the number of oscillations in the comb spectrum.

The spectrum of a normal DKS is distinctly different from the anomalous DKS. It displays a number of ripples that are somewhat linked to the ripples in the temporal field. Thus, the spectrum is much less even compared to the anomalous DKS. However, the conversion efficiency of these waveforms is usually higher than 20% [31], much higher than their anomalous GVD counterpart. This is mainly due to the fact that the normal DKS can be operated with the CW pump effectively located closer to center of resonance [31]. Much of this converted power is concentrated near the pump frequency, but Paper A showed that the overall comb-line power of the normal DKS was nonetheless higher than the anomalous DKS. This makes the normal DKS more attractive for optical telecommunication experiments, which is why they were employed in Papers I and M.

Demonstrations of normal DKSs typically require advanced dynamics for CW initiation. The problem lies in that the normal DKS cannot be initiated from a CW laser in a single-mode normal-GVD microring due to a lack of MI, as was discussed in section 4.1.3. Normal DKS thus require a perturbed GVD profile to achieve the phase matching required for MI, i.e. by employing an avoided mode-crossing [31, 158].

The first experimental demonstrations of a normal DKS generated by pumping a resonance in a mode-crossing enabled by two linearly-coupled guided modes in the same microring cavity [31, 158, 163]. These have been useful in demonstrating the dynamics of dark DKS, such as in Paper C, where it was shown that normal DKSs are generated deterministically by simply tuning a CW laser into resonance from the blue side. However, as discussed in section 3.2, the coupled waveguide modes offer limited control over the linear mode-coupling strength and location of the avoided mode-crossing. If either of these factors are not set correctly, a DKS might not be attainable. Furthermore, if the avoided mode-crossing is not tunable, a DKS is generally only achieved when pumping one specific resonance. This difficulty is perhaps the reason why normal DKS have not been used as commonly in demonstrations compared to the anomalous DKS.

Other efforts of normal DKS generation have featured linearly coupled microresonators, where the avoided mode-crossing can be moved separately via microheaters on each microring [130]. Microcombs from such a design were first demonstrated in [31], with [53] showing later

improvements. Paper D demonstrated unequivocally a DKS in linearly coupled microresonators, while uncovering distinctive dynamics such as an extended existence regime and normal DKS existence in absence of CW bistability. A more recent alternative to the linearly coupled microrings is to involve coupling to the CW laser cavity, which can result both in self-injection locking and initiation in the normal dispersion regime with remarkable reduction of frequency noise [55].

Microresonators support a wide range of DKS states and dynamics beyond the ones mentioned above. DKSs with oscillating temporal amplitude, often named breathers, have been observed in both the anomalous and normal GVD regime [166–168]. Higher order dispersion impacts the spectral shape of the DKS, which can introduce dispersive waves [169–171] and quartic solitons [172]. The Raman effect can cause a self-frequency shift to the DKS envelope [173,174] and enable the generation of Stokes solitons [175,176]. Soliton crystals can be generated in the anomalous-GVD with the assistance of a mode-crossing [30,177,178]. Such mode-crossings can be generated by employing photonic molecules, which is the topic of the next chapter.

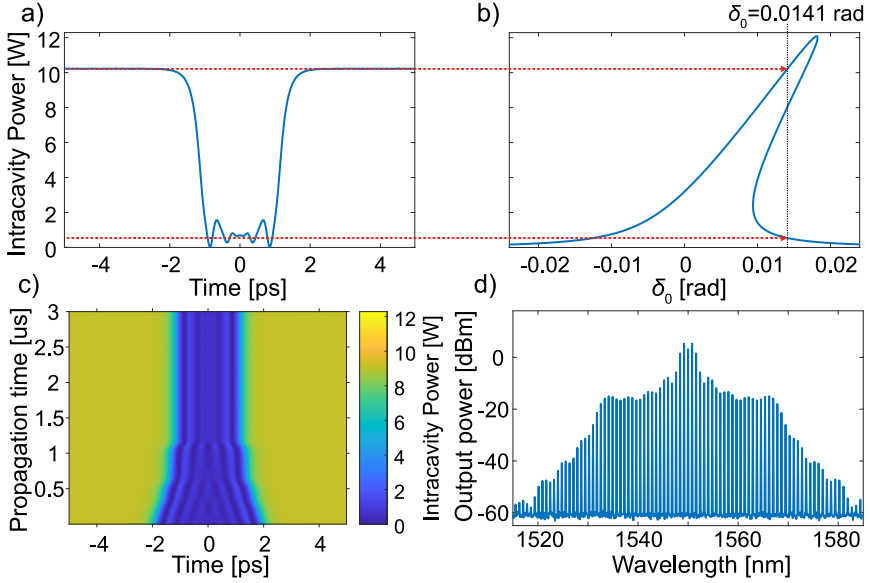


Figure 4.6: a) shows the temporal characteristics of a normal DKS in the form of a dark pulse circulating in a single-mode normal dispersion cavity. b) shows the bistability for the same cavity, with a vertical dashed line indicating the detuning at which the normal DKS operates. The red lines drawn between a) and b) show that the upper and lower power levels of the dark pulse are strongly linked to the upper and lower branch of the bistability, where the normal DKS can be considered to switch between. c) shows how the dark pulse is formed from an initial condition of a dark square pulse with amplitudes and phase corresponding to the CW bistability solutions. d) shows the spectrum that corresponds to the dark pulse. Parameters used were $\theta = 0.005$, $\beta_2 = 100 \text{ ps}^2/\text{km}$, $L = 1.5 \text{ mm}$, $FSR = 100 \text{ GHz}$, $\alpha = 0.5 \text{ m}^{-1}$, $\gamma = 1 \text{ (Wm)}^{-1}$, $\delta_0 = 0.0141$, $P_{in} = 20 \text{ mW}$.

Chapter 5

Nonlinear dynamics in photonic molecules

As the physics of a DKS generated in a single-mode cavity has steadily become better understood, the microcomb research field has been moving towards more complex systems, such as a microcomb-laser hybrids [62, 179], pulsed pumping [60, 180] and self-injection locking [46, 160]. Photonic molecules offer yet another approach to increase the complexity and enhance Kerr microcomb generation. These enhancements include: Causing a dispersive wave which can stabilize soliton crystals [30], reduce phase noise [181] and enable deterministic DKS generation [54, 129]; facilitate MI in the normal GVD allowing enhanced signal generation [182] and DKS initiation [31, 52, 158, 183, 184]; improve conversion efficiency [64, 183]; and introduce exotic DKS dynamics in diatomic photonic molecules [125, 185, 186], and cascaded microrings [124, 187]. Papers C-F provide extensive modelling and analysis of photonic molecules, focusing on comb initiation and conversion efficiency. Here, we provide extra analysis that further explain the dynamics in these papers. In the first section, we discuss CW steady-state solutions in photonic molecules, and how the relative locations of the resonances effect comb generation. In the second section, we discuss the validity of applying a fixed frequency shift to a pumped resonance to emulate the coupling interaction with an auxiliary cavity. In the third section, we show how a shifted pump resonance allows DKS initiation in the normal dispersion regime.

5.1 Power buildup in Kerr-nonlinear photonic molecules

To analyze Kerr nonlinear photonic molecules, we combine the LLE (equation 4.5) with the coupled mode formalism from equation 3.16 [183, 184], resulting in

$$\begin{aligned}\frac{\partial A_1}{\partial z} &= (-\sigma_1/L - i\delta_1/L - i\frac{\beta_2^{(1)}}{2}\frac{\partial^2}{\partial t^2} - i\gamma_1|A_1|^2)A_1 + i\kappa_z A_2 + i\sqrt{\theta}A_{in}/L \\ \frac{\partial A_2}{\partial z} &= (-\sigma_2/L - i\delta_2/L - d\frac{\partial}{\partial t} - i\frac{\beta_2^{(2)}}{2}\frac{\partial^2}{\partial t^2} - i\gamma_2|A_2|^2)A_2 + i\kappa_z A_1,\end{aligned}\tag{5.1}$$

where A_1 and A_2 are the temporal fields of cavity 1 (main) and 2 (auxiliary). The walk-off factor, d , signifies the offset group velocity between the two cavities. Note that cross-phase modulation is sometimes added between A_1 and A_2 when their geometrical mode-space significantly overlap. Assuming CW steady-state conditions, we greatly simplify these equations as

$$\begin{aligned}0 &= (-\sigma_1/L - i\delta_1/L - i\gamma_1|A_1|^2)A_1 + i\kappa_z A_2 + i\sqrt{\theta}A_{in}/L \\ 0 &= (-\sigma_2/L - i\delta_2/L - i\gamma_2|A_2|^2)A_2 + i\kappa_z A_1.\end{aligned}\tag{5.2}$$

The fact that we have Kerr nonlinearity in both cavities makes this system significantly more complex compared to the single-mode case in equation 4.6, supporting up to 9 steady-state solutions. Such features have been studied in numerous coupled cavity systems [183, 188–190]. Here, we use these equations to examine the power buildup in the photonic molecule resonances. This helps us understand how we should configure our photonic molecule resonances in order to get microcomb generation in the main cavity.

The comb generation in Papers D-F relied on the pumping of a resonance which was red-shifted due to coupling interaction with the auxiliary cavity. Figure 5.1a, shows an example of how the CW steady-state power would typically look like for such an arrangement. Relatively low CW power was used, which only leads to bistable resonance-splits. The red-shifted resonance has significantly more buildup of power in the main cavity compared to the auxiliary cavity. This difference is enabled by the fact that the uncoupled auxiliary resonance (marked by a green dotted

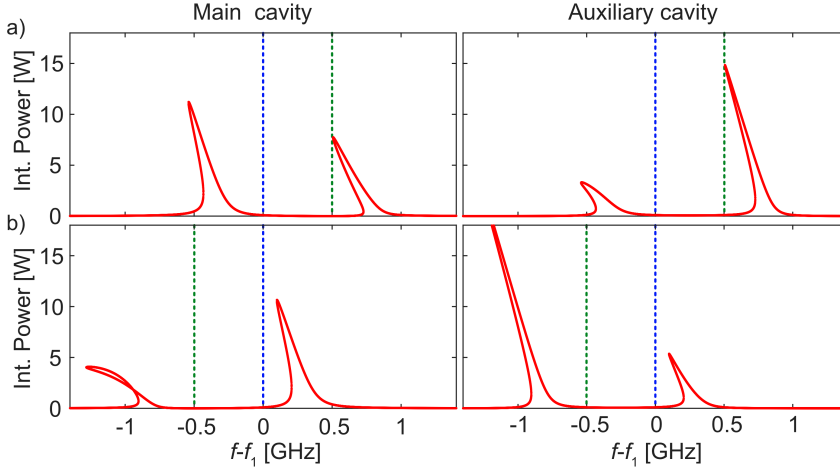


Figure 5.1: The CW steady-state solutions for the nonlinear coupled cavities for two different configurations. The left (right) column shows the main (auxiliary) intracavity power. The blue (green) dashed line shows the resonance location of the main (auxiliary) mode in absence of coupling (i.e. $\kappa_z = 0$). a) shows has the uncoupled auxiliary mode shifted 0.5 GHz towards the blue side compared to the uncoupled main mode. b) has the auxiliary mode shifted to the red side by the same amount. The CW laser frequency is given by f , with f_1 being the location of the uncoupled main resonance. Parameters used for the steady state solutions were $P_{in} = 20 \text{ mW}$, $\theta = 0.005$, $L = 1.5 \text{ mm}$, $FSR_1 = 100 \text{ GHz}$, $FSR_2 = 104 \text{ GHz}$, $\alpha_1 = \alpha_2 = 0.5 \text{ m}^{-1}$, $\gamma_1 = \gamma_2 = 1 \text{ (Wm)}^{-1}$, $\kappa_z = 20.54 \text{ rad/m}$

line in the figure) is slightly blue shifted compared to the main resonance. This difference in power level means that comb generation can be enabled in the main cavity while the auxiliary cavity remains under MI threshold. If we tune the uncoupled auxiliary resonance to the red side of the uncoupled main resonance, the situation is reversed, with the red-shifted resonance having dominant power buildup in the auxiliary cavity (see figure 5.1b). This configuration enables DKS generation in the auxiliary cavity [64,183]. It is for this reason that the DKS dynamics in Papers C-F all required the auxiliary resonance to be located on the blue side of the main resonance. It also underlines the need for the cavity heaters in Papers D-F, which helped configuring these power dynamics to ensure comb generation in the main cavity.

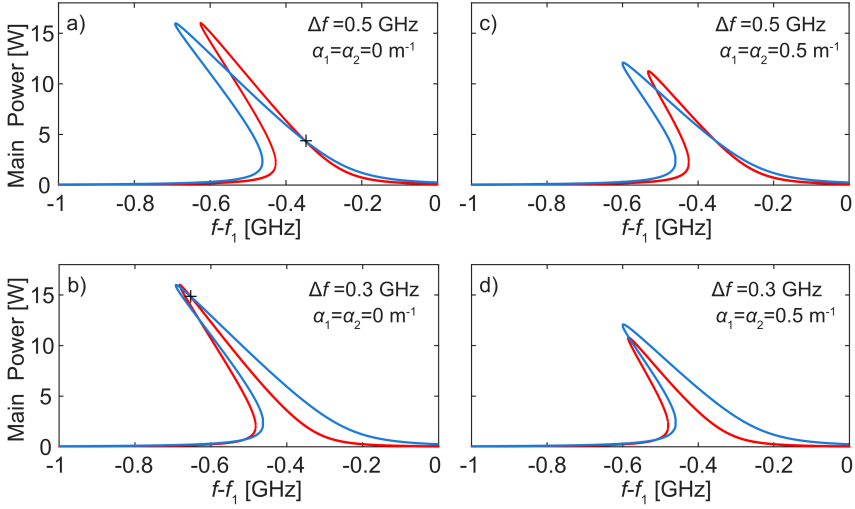


Figure 5.2: The CW steady-state solutions for of the main cavity when considering a photonic molecule configuration (red) and a single cavity resonance with a constant resonance shift (blue). The offset between the uncoupled auxiliary resonance and uncoupled main resonance is given by (Δf) . In a-b) we consider no intrinsic losses, with Δf being the only difference between the two figures. The cross marks the frequency where the two configurations give the same solution. In c-d) show the same as a-b), but with intrinsic included in all cavities. Other parameters are the same as in figure 5.1a.

5.2 Replacing the auxiliary cavity with a constant frequency shift

From the viewpoint of the main cavity, the interaction with the auxiliary cavity can be approximated as frequency shift applied to the main cavity mode. This approach was extremely useful in Paper F to investigate the conversion efficiency dynamics of photonic molecules, where for each simulated DKS state generated in a photonic molecule we could typically replace the auxiliary cavity with a constant phase shift applied to the pump per roundtrip. However, we cannot consider the fixed resonance shift as a complete replacement for the photonic molecule dynamics. To illustrate this, in figure 5.2, we compare the the main cavity CW-steady state solutions of a single resonator with a fixed resonance shift. Figure 5.2a, which includes no intrinsic losses, shows that the single-cavity with a fixed resonance shift qualitatively matches the photonic molecule, but

it is not a one-to-one match. In fact, ignoring the unstable middle branch, the two systems only show an exact match for one frequency. This is because the shift introduced auxiliary cavity is dynamical, depending on offset between the uncoupled longitudinal modes of the two cavities. This offset effectively increases as power builds up in the main cavity due to the nonlinear phase shift, which in turn decreases impact from the auxiliary cavity. This effect can be countered by simply moving the position of the auxiliary longitudinal modes (see figure 5.2c), allowing a match between the two systems at other laser frequencies.

In figures 5.2c-d, we add intrinsic losses to the cavities. Now we also see a mismatch in power between the shifted single-cavity and the photonic molecule. This is due to the fact that the auxiliary cavity introduce not only a frequency shift, but also extra losses from the viewpoint of the main cavity. This underlines the importance of realizing high-Q cavities.

5.3 DKS initiation in the normal dispersion regime

The method of red-shifting the pump resonance to approximate the impact of the auxiliary cavity was used in Paper F to analyze the phase-matching and parametric amplification. The same mechanism can also enable DKS generation in the normal dispersion regime [31, 158, 164]. Here, we do a brief analysis of the initiation of normal GVD microcombs with a red-shifted resonance. The analysis is similar to previous work [158], where the comb detuning (as defined in paper F) is linked to the parametric gain conditions introduced in section 4.1.3. For this, we consider a single cavity with the parameters defined in figure 4.6. The CW pump frequency is scanned into resonance from the blue side towards the red side while recording the peak intracavity power and conversion efficiency. In addition, we record the threshold conditions for parametric gain as described in section 4.1.3, which are repeated here for convenience:

$$\Delta\Omega_m^2 = 2\frac{\delta_c - 2\gamma LP}{\beta_2 L}, \quad P_{th} = \sigma/(\gamma L), \quad (5.3)$$

where δ_c is the comb detuning. According to these equations, a parametric gain is possible where $\Delta\Omega_m^2 > 0$ and $P > P_{th}$, where P is the intracavity power. The results of the simulations are displayed in figure 5.3. Figure 5.3a-b displays a build up of power as the laser is scanned

into resonance shifted by 0.002 radians per roundtrip, with rise in conversion efficiency showing where a comb is eventually generated. The comb initiation is only realized where both of the parametric gain conditions are met, suggesting that the equations above do indeed predict the conditions for DKS initiation in the normal GVD regime. Note however that the existence regime of the DKS is rather narrow, which would make it hard to obtain in practice. The red-shift of the pump resonance is now increased to 0.01 radians per roundtrip (figure 5.3c-d). This eases the parametric gain conditions, allowing the DKS comb to be initiated at a much lower intracavity power and providing larger existence range. These results suggest that the comb initiation in normal dispersion resonators with shifted pump resonance is indeed predicted by the parametric gain conditions. It also suggests that the key mechanism in the extended existence of normal DKSs in paper D was enabled by the strong red-shift of the pumped resonance.

The DKS's temporal power distribution and spectral distribution is displayed in figure 5.3e-f. These waveforms are symmetric, similar to the DKSs in reference [164], which employed a similar approach of pump resonance shift. Such waveforms can in principle be realized experimentally using normal GVD photonic molecule configuration with a mismatch in microring sizes, similar to paper F. This is demonstrated in appendix A.

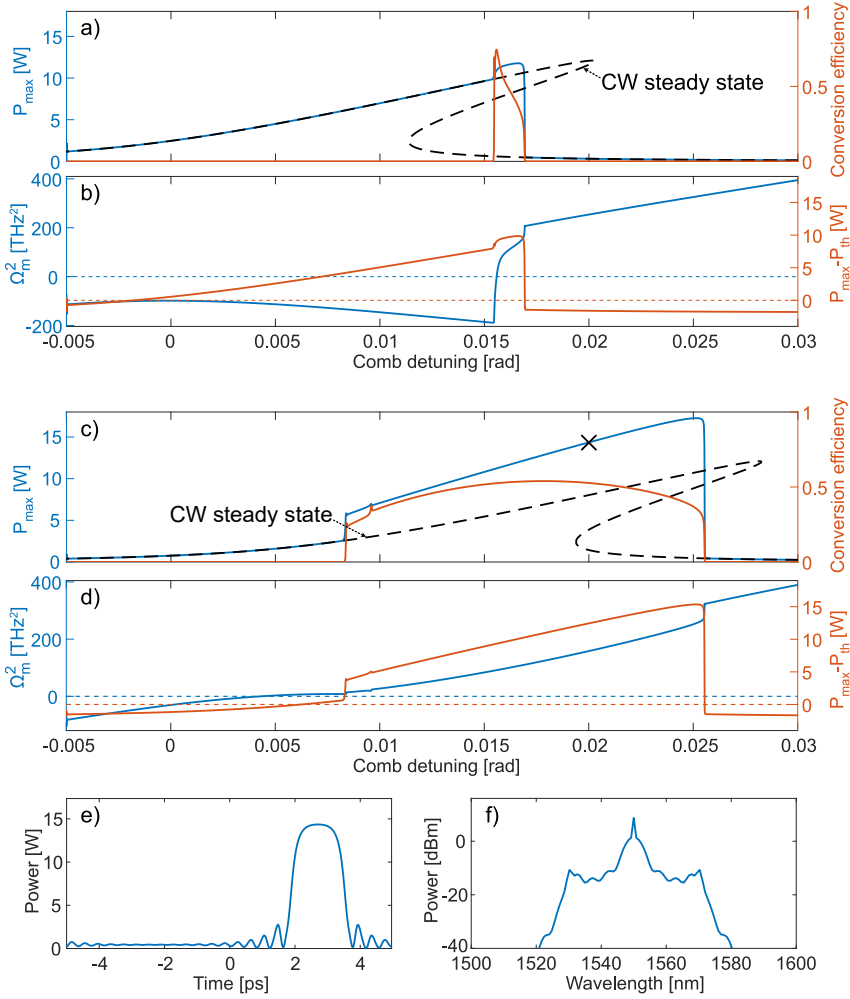


Figure 5.3: a) shows the a laser frequency scan into pump resonance which has been red-shifted by 0.002 radians per roundtrips. It displays the peak intracavity power (P_{max}), conversion efficiency and the CW steady state solutions. b) shows the corresponding phase-matched frequency Ω_m and the difference between threshold power and peak intracavity power. The thresholds of each axis are indicated by the dashed lines. c-d) are the same as a-b, only with a red-shift of 0.01 radians per roundtrip. The intracavity DKS state marked by 'x' is shown in e) with the corresponding output spectral envelope shown in f).

Chapter 6

Future outlook

This thesis has focused on the study of DKS dynamics in microresonators, with emphasis on linearly coupled cavities and high efficiency microcombs. Here, I highlight some areas that in my opinion deserve to be explored in the future.

- Papers A-B investigated the scaling of conversion efficiency of DKSs in single-cavity microresonators, showing that the normal dispersion has a slight benefit over the anomalous dispersion in terms of power-per-line. With the introduction of photonic molecules in Papers D-F, new dynamics are added which affect the scaling of comb power. The practical limitations of such enhancements have not been defined so far, and it is unclear if the normal dispersion or anomalous dispersion will be ultimately more beneficial. It would be interesting to resolve these uncertainties with a numerical study.
- The dynamics of the photonic molecule system is considerably more complicated than the single-mode system. For example, apart from the improved conversion efficiency, we found exotic dynamics such as DKS initiation with backwards scanning of the CW laser, DKS operation with the CW laser detuned to either side of pump resonance and extended existence regimes in terms of detuning and pump power. The parameter space of such photonic molecules has not been fully explored, and other useful dynamics are potentially yet to be discovered in such structures.
- The simple idea of shifting the pumped resonance to improve conversion efficiency presented in Paper F could in principle be im-

plemented in systems other than the photonic molecules, e.g. interaction with a laser cavity or coupling to other frequency modes via harmonic generation. It would be interesting to do a numerical study, preferably supported by experimental evidence, to demonstrate that this conversion efficiency enhancement is indeed universal and can occur in multiple different systems.

- Some of the previous work in the microcomb research field has involved co-integration of microresonators with lasers [48], with self injection locking of the pump laser to the soliton microcomb [46, 47]. Other studies have involved co-integration of other optical components [49], aiming at fully integrated microcomb systems [37, 49, 50]. The improved power efficiency demonstrated in Papers D-F would be useful in such co-integration schemes as it can relax the requirements in terms of laser power, optical losses and photodiode sensitivity. A demonstration of high-efficiency DKS co-integrated with other optical components would be an interesting future project.
- The photonic molecule demonstrated in Papers D-F had high efficiency, typically covering a 20-80 nm span around the 1550 nm pump. To achieve self-referencing, this bandwidth would need to be extended by an order of magnitude to reach an octave span. A demonstration of an reproducible octave spanning microcomb with dramatically improved conversion efficiency would be of interest for microcomb community in general.

Chapter 7

Summary of Papers

Paper A

Superchannel engineering of microcombs for optical communications,

Journal of the Optical Society of America B, 36, 8, 2013-2022, 2019.

Here, we conduct a numerical investigation into the performance of DKSs in both normal and anomalous dispersion single-mode cavities for generating frequency carriers for fiber optical communications. We discuss the benefits of using multiple narrow microcomb sources, each constituting a superchannel, compared to using a broad microcomb source. We discover that the line power of anomalous and normal DKSs follow the same scaling in terms of input power and number of lines generated, showing that normal DKSs can offer up to 3 dB higher line power compared to the anomalous DKS.

My contributions: I conducted the simulations, I wrote the paper with support from co-authors, I presented the work at CLEO 2018

Paper B

Laser Frequency Combs for Coherent Optical Communications,

Journal of Lightwave Technology, 37, 7, 1663-1670, 2019.

In this work, we explore the benefits and tradeoffs of using frequency combs in optical communications. The study involves

data-link performance with regards to important comb characteristics, such as line power, linewidth and line spacing. Furthermore, we discuss how the coherence can be utilized to simplify the hardware of the data receiver. Finally we compare the performance of electro-optic combs with microresonator combs in terms of minimum line power.

My contributions: I conducted the microcomb simulations in the last section of the paper.

Paper C

Switching dynamics of dark-pulse Kerr comb states in optical microresonators,

Physical Review A, 103, 1, 013513, 2021.

In this work, we investigate the dynamics of DKS comb generation in the normal dispersion regime, both experimentally and numerically. Spectrally probing the pump resonance as the DKS is generated, we discover that an extra resonance appears once the comb is initiated. We find that the two resonances are closely linked to the bistability of the cavity. We also find that the DKS spectrum exhibits switching between different states. Numerical simulations accurately replicated the comb spectra, showing that the different states correspond to dark pulses with different number of oscillations.

My contributions: I conducted single-mode simulations to verify the VNA scans, I assisted with lab measurements, I presented the part of the work that featured hot cavity spectroscopy at CLEO EU 2019.

Paper D

Dissipative Kerr solitons in photonic molecules,

Nature Photonics, 15, 4, 305-310, 2021.

Here, we demonstrate DKS generation in linearly-coupled normal dispersion microrings. Using a microheater on one of the rings to control the coupling interaction, we demonstrate that these structures can generate DKSs with high conversion efficiency at low input power in a reproducible manner. We show through numerical simulations

that the dynamics of these DKSs are enabled by the linear coupling of two cavities. We numerically demonstrate that this design offers DKSs with a larger existence regime compared to normal dispersion DKSs in single-mode cavities.

My contributions: I conducted the lab experiments, I simulated microcombs dynamics numerically, I assisted with numerical characterization, I wrote parts of the paper, I presented a part of the work at CLEO 2020.

Paper E

Bidirectional initiation of dissipative solitons in photonic molecules,

Conference on Lasers and Electro-Optics Europe and European Quantum Electronics Conference, ef_5_1, 2021.

We find that the photonic molecule configuration from Paper D allows initiation of solitons by tuning the CW laser into resonance from the red side. This is enabled by the fact that dissipative solitons exist on the blue side of cavity resonance in absence of bistability.

My contributions: I conducted the lab experiments and numerical simulations. I presented the work at CLEO EU 2021.

Paper F

Power efficient soliton microcombs,

Submitted to a journal, preprint available at arXiv:2202.09410

We demonstrate a single DKS in an anomalous cavity with vastly improved conversion efficiency with excellent phase noise stability. This was achieved by shifting of the pumped resonance in the DKS cavity using a photonic molecule arrangement. The dynamics were demonstrated both experimentally and in numerical simulation. Other interesting dynamics, such as operating a soliton below the modulational instability limit, backwards initiation and operating the soliton with the CW laser blue detuned to the pumped resonance.

My contributions: I came up with idea, conducted the lab experiments and numerical simulations. I wrote large portions of the paper.

Appendices

Appendix A – Initiation of DKS states in photonic molecules

DKSs can be generated in linearly coupled microresonators in fairly reliable manner by using a CW laser in combination with cavity heaters. The purpose of this section is to provide a technical guide for finding and initiating DKS states in photonic molecule microresonators.

General setup

It is important when working with microresonator chips to have a stable environment with minimal fluctuation in temperature and a steady coupling of optical power to the chip. In this work, the chip is placed on a temperature controlled surface (see figure 7.1a). This allows us to maintain a constant temperature of the overall chip which reduces the impact of temperature drifts in the environment that might cause the resonances to drift in frequency location. The chip is typically fixed place, e.g. by using vacuum suction or by clamping it down with an elastic material. The heater circuits of the microrings are coupled to a power supply using probes. Typically, the voltage resolution of the power supply should be in the range of 1 mV, with the ability to apply up to 500 mW of electrical power to the circuit. The waveguides on the chip are optically coupled using lensed fibers, with typical coupling losses of 1.5-3 dB per facet.

To characterize the initiation of DKSs, we need a setup which allows us to control the frequency location of the CW pump laser relative to the resonances of the photonic molecule. We also need a way to monitor the resonances and the converted power of the DKS states. Figure 7.1b shows a typical setup which can be used to find DKS states. It involves a CW laser which can be tuned in wavelength, e.g. using a piezo actuator. A polarization controller is used to adjust the polarization of the laser

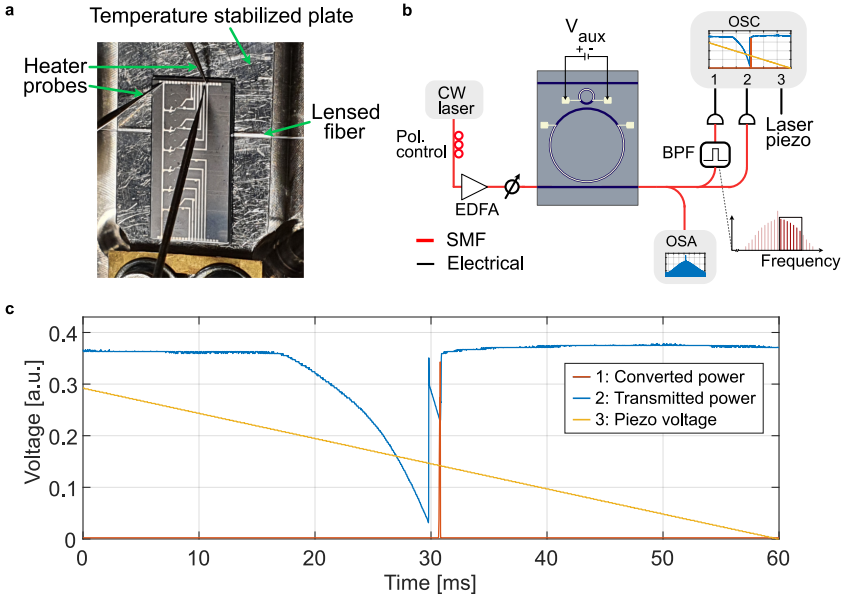


Figure 7.1: a) shows a chip which contains microresonators coupled to lensed fibers and heater probes. The chip is placed on a metallic plate which is temperature stabilized. b) shows a typical setup for microcomb generation. In this example the CW laser is swept in wavelength by applying a ramp function to a piezo actuator in the laser cavity. A voltage V_{aux} is applied to the auxiliary heater. The output of c) shows the oscilloscope response as the piezo voltage is linearly tuned down, which approximately corresponds to a linear scan in frequency from the blue side towards the red. The frequency scan speed is roughly 0.2 GHz/ms in this case. The transmitted power and converted power are proportional to the measured voltage.

to match the desired polarization of the resonator. A combination of an erbium doped fiber amplifier (EDFA) and a tunable attenuator are employed to control the input laser power. A portion of the output from the microresonator is coupled to an optical spectrum analyzer (OSA) to monitor the spectrum of generated microcombs. The throughput is also detected in an oscilloscope (OSC) using a photodiode. This allows us to observe the resonances of the microcavity as we scan the laser frequency. The converted power is also recorded in the oscilloscope, allowing us to monitor if a comb is being generated during laser frequency scans. This requires an optical filter that suppresses the laser frequency, but allows the frequencies of generated comb lines to be passed through.

The passband of this filter can be configured in a variety of ways, e.g. as a notch filter which suppresses only the pump or a bandpass filter which passes a selected portion of the comb spectrum. The control voltage for the CW laser frequency tuning (e.g. piezo voltage) is typically measured in the oscilloscope to give a reference for the direction of the frequency scan. Although not included here, it is also useful to measure the frequency scanning of the laser, e.g. using beating with a self-referenced laser as was done in Paper D-F.

Figure 7.1c, shows a typical oscilloscope reading when scanning the laser frequency across the resonance from the blue side towards the red. It shows the decrease in piezo voltage, which indicates an increase in wavelength. It also shows resonances in the transmitted trace, and a rise in converted power, which indicates comb generation. This trace allows us to verify if there are comb states being generated, and how far into the resonances we need to tune to attain them.

To demonstrate how we can use this system for DKS generation, we look at an example of a normal-GVD photonic molecule in the next section.

DKS initiation using a normal-GVD photonic molecule

Here we look into the initiation of a DKS in normal-GVD linearly-coupled microrings. For this demonstration, we use a design with microrings of vastly mismatched sizes. The main cavity has near 50 GHz FSR while the auxiliary cavity has an FSR near 480 GHz. This will enable similar dynamics as in section 5.3, where we only induce a shift to the pumped resonance. The procedure to generate DKSs in this configuration is similar to the arrangement of similar sized rings used in Paper D. Prior to high power pumping, this device had been characterized with high intrinsic Q factors (>5 million) with most of the resonances having a Lorentzian profile. This characterization is an important step, since low intrinsic Q can impede the DKS generation, especially when scattering causes coupling to the counter-propagating mode. It is also important to verify that the heaters work by measuring the resistance across the heater circuit, and by testing that resonances of the cavities shift when applying voltage to the heater circuit. The power across the heaters should be kept below 500 mW to reduce the chances of a burning the circuit.

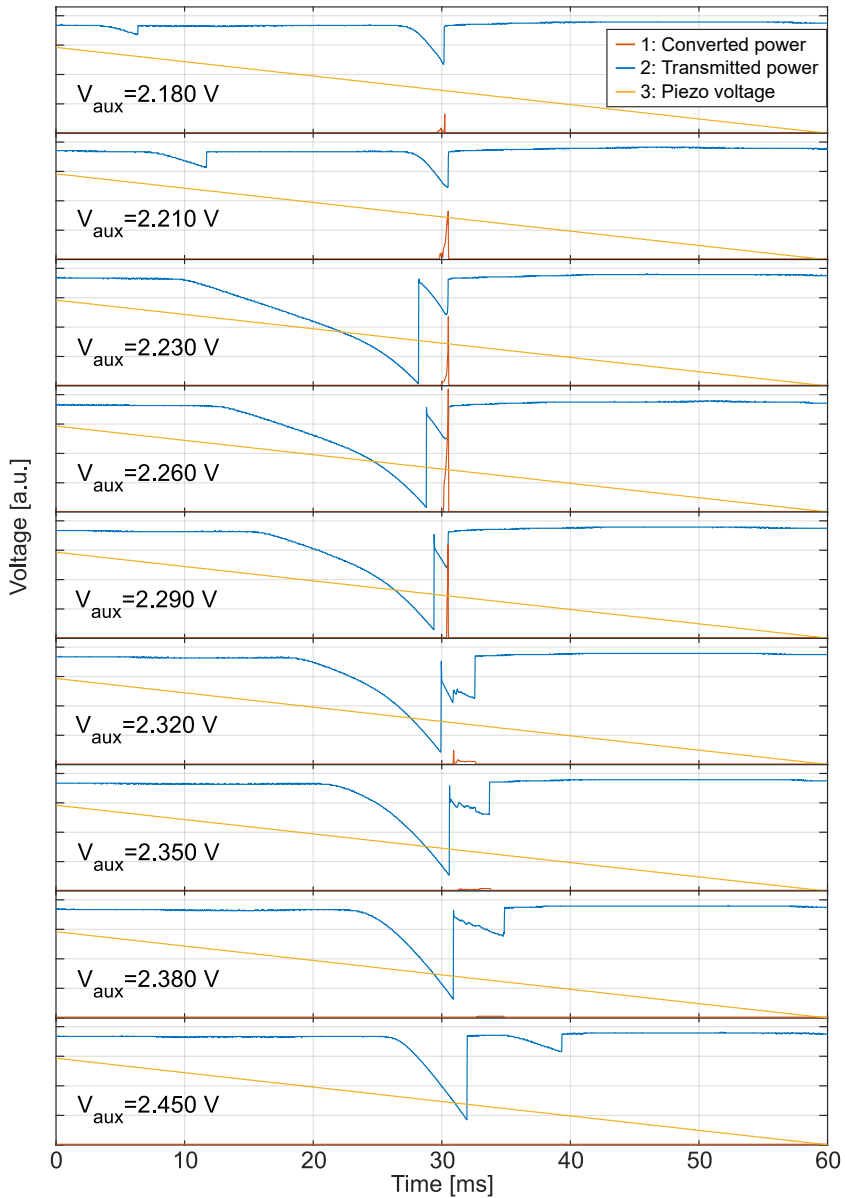


Figure 7.2: The response of the laser frequency scan as the auxiliary resonance is tuned across the main resonance by increasing the auxiliary heater voltage. The laser frequency is reduced by approximately 2 GHz in a 10 ms time span.

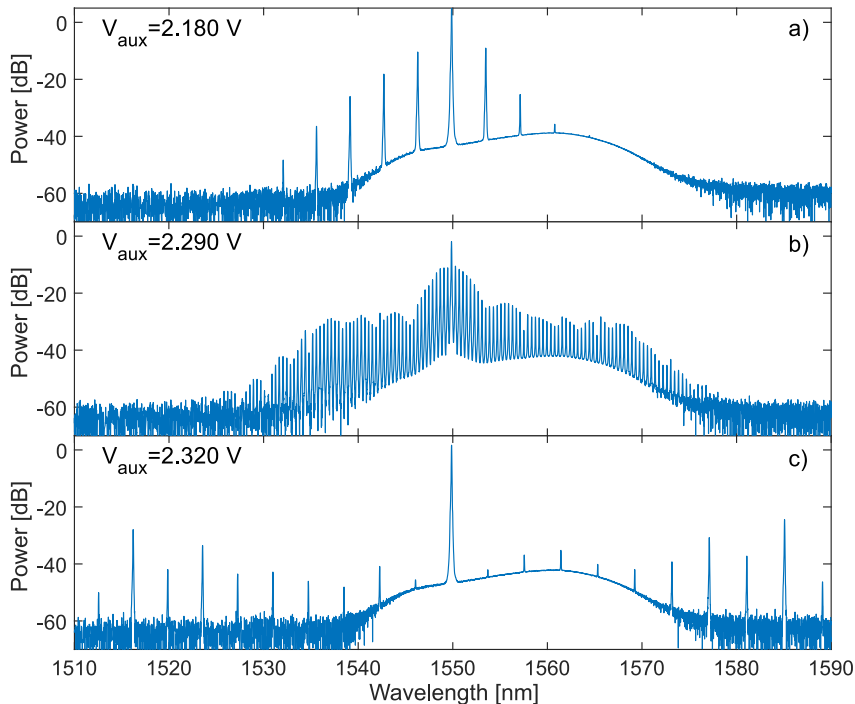


Figure 7.3: Comb states found when tuning into the resonances at the indicated auxiliary resonance voltages. The configuration of the cavities is the same as the frequency scans in figure 7.2 which have the same auxiliary voltage.

Having identified the quality of the sample, we place it in the setup of figure 7.1. We turn the laser frequency scan on, and tune the center of the frequency scan (or tune the voltage of the main cavity heater) until we see a resonance in the transmitted trace in the oscilloscope. Now we tune the auxiliary heater voltage until a second resonance appears in the oscilloscope (see figure 7.2). We tune the auxiliary resonance across the main resonance and observe the changes in transmitted power and converted power. If no converted power is observed, then we increase the input CW power. As a rule of thumb, the DKSs are easiest to find when setting the laser 5-10 dBm above MI threshold.

Having established that we can tune the auxiliary resonance across the main resonance, with clear indications of converted power in the oscilloscope, it is now time to attempt DKS initiation. The aim is to bring the auxiliary resonance into close proximity to the main resonance, caus-

ing the main resonance to red-shift. This is the key ingredient to DKS initiation in the normal dispersion regime, as was discussed in section 5.3. For this, we want to investigate an auxiliary voltage span starting from a point where the auxiliary resonance is far on the blue side compared to the main resonance, and ending at a spot where the two resonances have a minimal distance between each other. This would correspond to voltages 2.18V-2.32V in figure 7.2. The process is simply to fix the auxiliary voltage, turn off the laser frequency scan, and tune the laser slowly into resonance from the blue side towards the red until a comb state is generated. This is repeated for the different auxiliary voltages, while maintaining a fixed main heater voltage, until we have good picture of what comb states are generated as the interaction between the two cavities is changed.

In figure 7.3, we show three comb states using three different configurations using 2.18V, 2.29V and 2.32V applied to the auxiliary cavity, each corresponding to the frequency scan of equal voltage in figure 7.2. At 2.18V, we have the auxiliary resonance located far on the blue-side of the main cavity, which results in a multi-FSR comb. For the CW initiation at 2.29V we have the auxiliary resonance pushed much closer to the main resonance, which increases the interaction of the two resonances causing a mode-split. The red-shifted resonance has more power buildup in the main cavity, and enough red-shifting to allow a single-DKS with a spectral envelope similar to figure 5.3f-e. At 2.32V, we have pushed the auxiliary resonance too far, such that the CW initiation leads to comb generation in the auxiliary cavity. This is due to the fact that the red-shifted resonance in the mode-split corresponds to dominant power buildup in the auxiliary cavity, as was discussed in section 5.1.

These examples show that single-DKS generation in the normal dispersion photonic molecules can be generated by tuning the CW laser into the red-shifted resonance of the mode-crossing. Note however that the exact configuration of the mode-crossing may differ from one photonic molecule design to another. For example, the single-DKS generation demonstrated in the supplementary of Paper D had a different separation between the two resonances.

In some cases, the a single-DKS is not attainable by just tuning the laser into resonance in the manner described here. Thankfully, we can apply another approach in such cases, demonstrated in figure 7.4. Essentially, we initiate a multi-FSR comb with the auxiliary resonance further towards the blue side of the main resonance. We then fix the laser

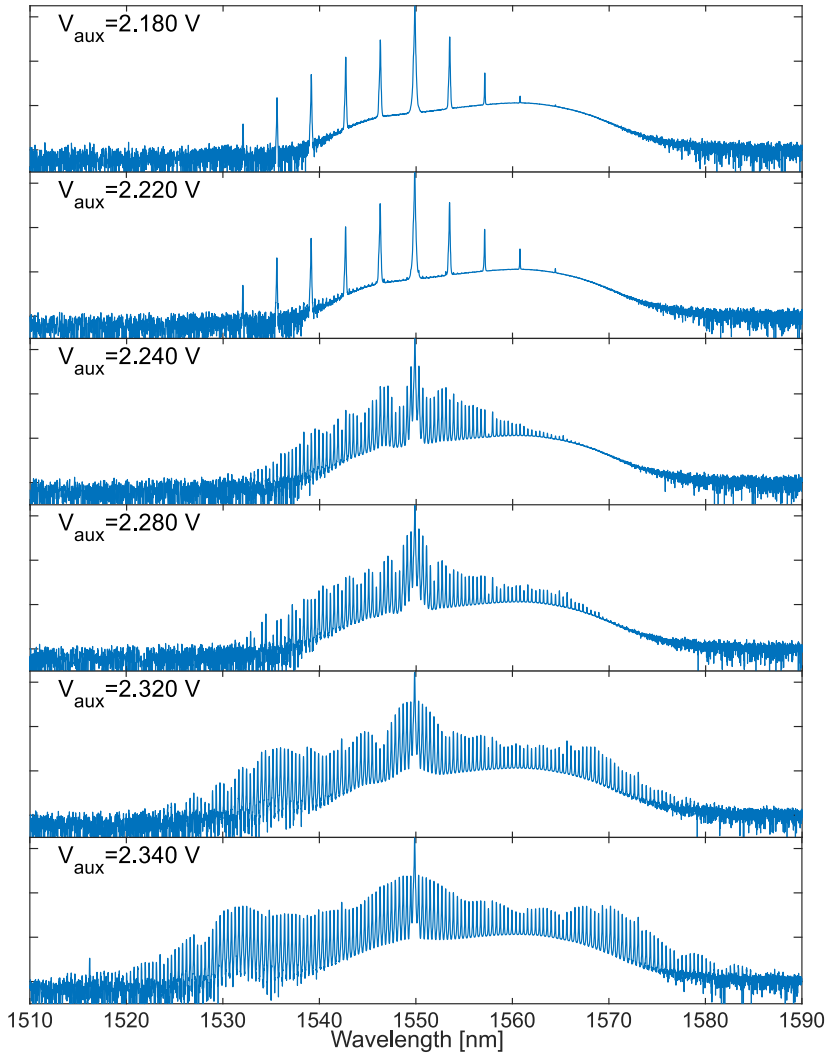


Figure 7.4: Tuning the auxiliary resonance closer to the main resonance allows a multi-FSR comb state (top figure) to be turned into a single-DKS state

frequency and tune the auxiliary heater voltage, inducing the desired redshift to the pumped resonance. This allows the comb state to gradually change from from a multi-FSR state to a single-DKS state. Such an approach was demonstrated in a previous paper [52], using two cavities of similar sizes. Note that in some cases, the laser frequency (or main

cavity heater) has to be tuned in unison with the auxiliary heater voltage to end up with the desired DKS state.

Finally, it is worth mentioning that these are not the only methods to attain DKS states in normal-dispersion photonic molecules. Paper E demonstrated backwards initiation, which was also a viable option for the sample tested here. CW initiation can also be done with a fixed laser frequency, tuning the heaters of the main and auxiliary cavity to modify the detuning between laser and resonances. The use of feedback to the laser frequency (or cavity heaters) to lock the comb power can also be useful when initiating the DKS [191,192]. It allows us counteract thermal shifts which often occur when going from one soliton state to another.

DKS initiation using an anomalous-GVD photonic molecule

The DKS initiation in photonic molecules using anomalous dispersion requires us to find a main cavity resonance which interacts with an auxiliary resonance. For this we follow steps similar to the normal dispersion regime, where we scan the auxiliary resonance across the main cavity and observe how it affects the comb initiation. In contrast to the normal dispersion, shifting the pumped resonance typically obstructs comb initiation. Thus, we initiate a comb with the auxiliary resonance far away from the main cavity, and only tune the auxiliary resonance close to the main resonance after comb initiation to reach a single DKS, as was discussed in Paper F.

In figure 7.5, we show an initiation process in an anomalous photonic molecule with a similar design as the devices in Paper F. Figure 7.5a shows the oscilloscope of the laser frequency sweep, revealing a large separation between the resonances of the two cavities, with a comb state generated in the main resonance on the red-side. By stopping the laser frequency sweep, and tuning the laser slowly into resonance from the blue side towards the red, we initiate the first comb state displayed in figure 7.5b. This state has the characteristics of a multi-DKS state. To reduce the number of DKSs in the cavity, we tune the auxiliary voltage such that the auxiliary resonance shifts closer to the main resonance. The increased interaction between the resonances allow the number of DKSs in the cavity to be reduced until we arrive at a single DKS state. The laser frequency and the main heater voltage can often be maintained

fixed during this process. In other cases, the laser frequency or main heater voltage have to be manipulated to allow the transition to a single DKS state. Locking the converted power to a fixed value using feedback to the laser frequency (or main cavity heater) can be useful in these cases, as it allows the laser frequency to be shifted automatically as the auxiliary voltage is tuned.

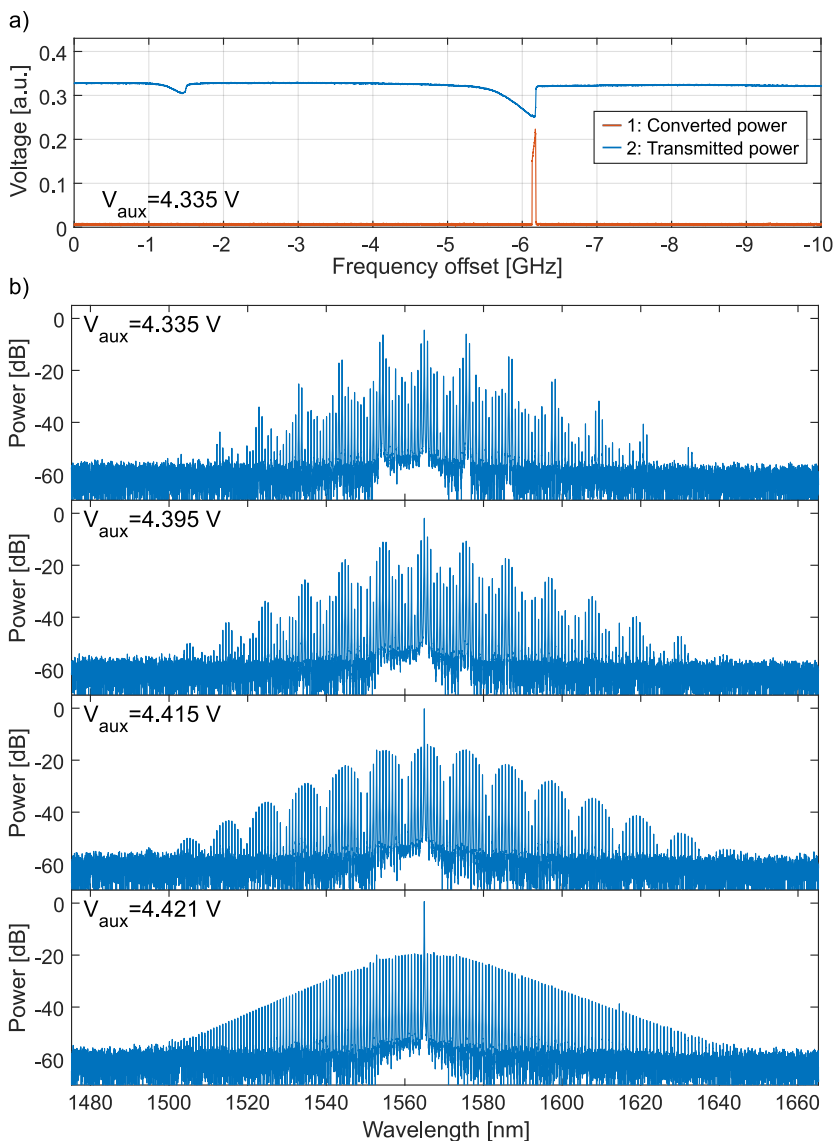


Figure 7.5: a) shows an oscilloscope measurement of a laser frequency scan probing an anomalous-dispersion photonic molecule. The frequency offset shows the change in laser frequency. b) shows the evolution of the generated comb-state as the auxiliary voltage is gradually increased. The comb-state state at 4.335 V was attained by tuning the laser into resonance using the same configuration as in a).

References

- [1] J. L. Hall, “Nobel Lecture: Defining and measuring optical frequencies,” *Reviews of Modern Physics*, vol. 78, no. 4, pp. 1279–1295, 2006.
- [2] T. W. Hänsch, “Nobel Lecture: Passion for precision,” *Reviews of Modern Physics*, vol. 78, no. 4, pp. 1297–1309, 2006.
- [3] D. J. Jones, “Carrier-Envelope Phase Control of Femtosecond Mode-Locked Lasers and Direct Optical Frequency Synthesis,” *Science*, vol. 288, no. 5466, pp. 635–639, 2000.
- [4] R. Holzwarth, T. Udem, T. W. Hänsch, J. C. Knight, W. J. Wadsworth, and P. S. J. Russell, “Optical Frequency Synthesizer for Precision Spectroscopy,” *Physical Review Letters*, vol. 85, no. 11, pp. 2264–2267, 2000.
- [5] S. T. Cundiff and J. Ye, “Colloquium : Femtosecond optical frequency combs,” *Reviews of Modern Physics*, vol. 75, no. 1, pp. 325–342, 2003.
- [6] S. A. Diddams, K. Vahala, and T. Udem, “Optical frequency combs: Coherently uniting the electromagnetic spectrum,” *Science*, vol. 369, no. 6501, p. eaay3676, 2020.
- [7] S. M. Brewer, J.-S. Chen, A. M. Hankin, E. R. Clements, C. W. Chou, D. J. Wineland, D. B. Hume, and D. R. Leibbrandt, “An $^{27}\text{Al}^+$ quantum-logic clock with systematic uncertainty below 10^{-18} ,” *Physical Review Letters*, vol. 123, no. 3, p. 033201, 2019.
- [8] R. A. McCracken, J. M. Charsley, and D. T. Reid, “A decade of astrocombs: recent advances in frequency combs for astronomy,” *Optics Express*, vol. 25, no. 13, p. 15058, 2017.

- [9] I. Coddington, N. Newbury, and W. Swann, “Dual-comb spectroscopy,” *Optica*, vol. 3, no. 4, pp. 414–426, 2016.
- [10] X. Xie, R. Bouchand, D. Nicolodi, M. Giunta, W. Hänsel, M. Lezius, A. Joshi, S. Datta, C. Alexandre, M. Lours, P.-A. Tremblin, G. Santarelli, R. Holzwarth, and Y. Le Coq, “Photonic microwave signals with zeptosecond-level absolute timing noise,” *Nature Photonics*, vol. 11, no. 1, pp. 44–47, 2017.
- [11] L. Lundberg, M. Karlsson, A. Lorences-Riesgo, M. Mazur, V. Torres-Company, J. Schröder, and P. Andrekson, “Frequency Comb-Based WDM Transmission Systems Enabling Joint Signal Processing,” *Applied Sciences*, vol. 8, no. 5, p. 718, 2018.
- [12] T. Fortier and E. Baumann, “20 years of developments in optical frequency comb technology and applications,” *Communications Physics*, vol. 2, no. 1, p. 153, 2019.
- [13] H. Haus, “Mode-locking of lasers,” *IEEE Journal of Selected Topics in Quantum Electronics*, vol. 6, no. 6, pp. 1173–1185, 2000.
- [14] L. E. Hargrove, R. L. Fork, and M. A. Pollack, “Locking of He–Ne laser modes induced by synchronous intracavity modulation,” *Applied Physics Letters*, vol. 5, no. 1, pp. 4–5, 1964.
- [15] V. Torres-Company and A. M. Weiner, “Optical frequency comb technology for ultra-broadband radio-frequency photonics,” *Laser & Photonics Reviews*, vol. 8, no. 3, pp. 368–393, 2014.
- [16] K. Beha, D. C. Cole, P. Del’Haye, A. Coillet, S. A. Diddams, and S. B. Papp, “Electronic synthesis of light,” *Optica*, vol. 4, no. 4, pp. 406–411, 2017.
- [17] D. R. Carlson, D. D. Hickstein, W. Zhang, A. J. Metcalf, F. Quinlan, S. A. Diddams, and S. B. Papp, “Ultrafast electro-optic light with subcycle control,” *Science*, vol. 361, no. 6409, pp. 1358–1363, 2018.
- [18] L. Chang, S. Liu, and J. E. Bowers, “Integrated optical frequency comb technologies,” *Nature Photonics*, vol. 16, no. 2, pp. 95–108, 2022.

-
- [19] A. L. Gaeta, M. Lipson, and T. J. Kippenberg, “Photonic-chip-based frequency combs,” *Nature Photonics*, vol. 13, no. 3, pp. 158–169, 2019.
- [20] S. Liu, X. Wu, D. Jung, J. C. Norman, M. J. Kennedy, H. K. Tsang, A. C. Gossard, and J. E. Bowers, “High-channel-count 20 GHz passively mode-locked quantum dot laser directly grown on Si with 4.1 Tbit/s transmission capacity,” *Optica*, vol. 6, no. 2, pp. 128–134, 2019.
- [21] M. Zhang, B. Buscaino, C. Wang, A. Shams-Ansari, C. Reimer, R. Zhu, J. M. Kahn, and M. Lončar, “Broadband electro-optic frequency comb generation in a lithium niobate microring resonator,” *Nature*, vol. 568, no. 7752, pp. 373–377, 2019.
- [22] T. J. Kippenberg, A. L. Gaeta, M. Lipson, and M. L. Gorodetsky, “Dissipative Kerr solitons in optical microresonators,” *Science*, vol. 361, no. 6402, p. eaan8083, 2018.
- [23] T. J. Kippenberg, R. Holzwarth, and S. A. Diddams, “Microresonator-Based Optical Frequency Combs,” *Science*, vol. 332, no. 6029, pp. 555–559, 2011.
- [24] T. J. Kippenberg, S. M. Spillane, and K. J. Vahala, “Kerr-Nonlinearity Optical Parametric Oscillation in an Ultrahigh-Q Toroid Microcavity,” *Physical Review Letters*, vol. 93, no. 8, p. 083904, 2004.
- [25] P. Del’Haye, A. Schliesser, O. Arcizet, T. Wilken, R. Holzwarth, and T. J. Kippenberg, “Optical frequency comb generation from a monolithic microresonator,” *Nature*, vol. 450, no. 7173, pp. 1214–1217, 2007.
- [26] A. Pasquazi, M. Peccianti, L. Razzari, D. J. Moss, S. Coen, M. Erkintalo, Y. K. Chembo, T. Hansson, S. Wabnitz, P. Del’Haye, X. Xue, A. M. Weiner, and R. Morandotti, “Micro-combs: A novel generation of optical sources,” *Physics Reports*, vol. 729, pp. 1–81, 2018.
- [27] S. Wabnitz, “Suppression of interactions in a phase-locked soliton optical memory,” *Optics Letters*, vol. 18, no. 8, pp. 601–603, 1993.

- [28] F. Leo, S. Coen, P. Kockaert, S.-P. Gorza, P. Emplit, and M. Haelterman, “Temporal cavity solitons in one-dimensional Kerr media as bits in an all-optical buffer,” *Nature Photonics*, vol. 4, no. 7, pp. 471–476, 2010.
- [29] T. Herr, V. Brasch, J. D. Jost, C. Y. Wang, N. M. Kondratiev, M. L. Gorodetsky, and T. J. Kippenberg, “Temporal solitons in optical microresonators,” *Nature Photonics*, vol. 8, no. 2, pp. 145–152, 2014.
- [30] D. C. Cole, E. S. Lamb, P. Del’Haye, S. A. Diddams, and S. B. Papp, “Soliton crystals in Kerr resonators,” *Nature Photonics*, vol. 11, no. 10, pp. 671–676, 2017.
- [31] X. Xue, Y. Xuan, Y. Liu, P.-H. Wang, S. Chen, J. Wang, D. E. Leaird, M. Qi, and A. M. Weiner, “Mode-locked dark pulse Kerr combs in normal-dispersion microresonators,” *Nature Photonics*, vol. 9, no. 9, pp. 594–600, 2015.
- [32] Z. L. Newman, V. Maurice, T. Drake, J. R. Stone, T. C. Briles, D. T. Spencer, C. Fredrick, Q. Li, D. Westly, B. R. Ilic, B. Shen, M.-G. Suh, K. Y. Yang, C. Johnson, D. M. S. Johnson, L. Hollberg, K. J. Vahala, K. Srinivasan, S. A. Diddams, J. Kitching, S. B. Papp, and M. T. Hummon, “Architecture for the photonic integration of an optical atomic clock,” *Optica*, vol. 6, no. 5, pp. 680–685, 2019.
- [33] A. Fülöp, M. Mazur, A. Lorences-Riesgo, Ó. B. Helgason, P.-H. Wang, Y. Xuan, D. E. Leaird, M. Qi, P. A. Andrekson, A. M. Weiner, and V. Torres-Company, “High-order coherent communications using mode-locked dark-pulse Kerr combs from microresonators,” *Nature Communications*, vol. 9, no. 1, p. 1598, 2018.
- [34] M. Mazur, M.-G. Suh, A. Fulop, J. Schroder, V. Torres-Company, M. Karlsson, K. Vahala, and P. Andrekson, “High Spectral Efficiency Coherent Superchannel Transmission With Soliton Microcombs,” *Journal of Lightwave Technology*, vol. 39, no. 13, pp. 4367–4373, 2021.
- [35] P. Marin-Palomo, J. N. Kemal, M. Karpov, A. Kordts, J. Pfeifle, M. H. P. Pfeiffer, P. Trocha, S. Wolf, V. Brasch, M. H. Anderson, R. Rosenberger, K. Vijayan, W. Freude, T. J. Kippenberg,

- and C. Koos, “Microresonator-based solitons for massively parallel coherent optical communications,” *Nature*, vol. 546, no. 7657, pp. 274–279, 2017.
- [36] M.-G. Suh, Q.-F. Yang, K. Y. Yang, X. Yi, and K. J. Vahala, “Microresonator soliton dual-comb spectroscopy,” *Science*, vol. 354, no. 6312, pp. 600–603, 2016.
- [37] C. Bao, Z. Yuan, L. Wu, M.-G. Suh, H. Wang, Q. Lin, and K. J. Vahala, “Architecture for microcomb-based GHz-mid-infrared dual-comb spectroscopy,” *Nature Communications*, vol. 12, no. 1, p. 6573, 2021.
- [38] M.-G. Suh and K. J. Vahala, “Soliton microcomb range measurement,” *Science*, vol. 359, no. 6378, pp. 884–887, 2018.
- [39] P. Trocha, M. Karpov, D. Ganin, M. H. P. Pfeiffer, A. Kordts, S. Wolf, J. Krockenberger, P. Marin-Palomo, C. Weimann, S. Randel, W. Freude, T. J. Kippenberg, and C. Koos, “Ultrafast optical ranging using microresonator soliton frequency combs,” *Science*, vol. 359, no. 6378, pp. 887–891, 2018.
- [40] E. Obrzud, M. Rainer, A. Harutyunyan, M. H. Anderson, J. Liu, M. Geiselmann, B. Chazelas, S. Kundermann, S. Lecomte, M. Cecconi, A. Ghedina, E. Molinari, F. Pepe, F. Wildi, F. Bouchy, T. J. Kippenberg, and T. Herr, “A microphotonic astrocomb,” *Nature Photonics*, vol. 13, no. 1, pp. 31–35, 2019.
- [41] Y. He, Q.-F. Yang, J. Ling, R. Luo, H. Liang, M. Li, B. Shen, H. Wang, K. Vahala, and Q. Lin, “Self-starting bi-chromatic LiNbO₃ soliton microcomb,” *Optica*, vol. 6, no. 9, p. 1138, 2019.
- [42] J. Liu, G. Huang, R. N. Wang, J. He, A. S. Raja, T. Liu, N. J. Engelsen, and T. J. Kippenberg, “High-yield, wafer-scale fabrication of ultralow-loss, dispersion-engineered silicon nitride photonic circuits,” *Nature Communications*, vol. 12, no. 1, p. 2236, 2021.
- [43] Z. Ye, K. Twayana, P. A. Andrekson, and V. Torres-Company, “High-Q Si₃N₄ microresonators based on a subtractive processing for Kerr nonlinear optics,” *Optics Express*, vol. 27, no. 24, p. 35719, 2019.

- [44] M.-G. Suh and K. Vahala, “Gigahertz-repetition-rate soliton microcombs,” *Optica*, vol. 5, no. 1, p. 65, 2018.
- [45] X. Liu, Z. Gong, A. W. Bruch, J. B. Surya, J. Lu, and H. X. Tang, “Aluminum nitride nanophotonics for beyond-octave soliton microcomb generation and self-referencing,” *Nature Communications*, vol. 12, no. 1, p. 5428, 2021.
- [46] B. Stern, X. Ji, Y. Okawachi, A. L. Gaeta, and M. Lipson, “Battery-operated integrated frequency comb generator,” *Nature*, vol. 562, no. 7727, pp. 401–405, 2018.
- [47] B. Shen, L. Chang, J. Liu, H. Wang, Q.-F. Yang, C. Xiang, R. N. Wang, J. He, T. Liu, W. Xie, J. Guo, D. Kinghorn, L. Wu, Q.-X. Ji, T. J. Kippenberg, K. Vahala, and J. E. Bowers, “Integrated turnkey soliton microcombs,” *Nature*, vol. 582, no. 7812, pp. 365–369, 2020.
- [48] C. Xiang, J. Liu, J. Guo, L. Chang, R. N. Wang, W. Weng, J. Peters, W. Xie, Z. Zhang, J. Riemensberger, J. Selvidge, T. J. Kippenberg, and J. E. Bowers, “Laser soliton microcombs heterogeneously integrated on silicon,” *Science*, vol. 373, no. 6550, pp. 99–103, 2021.
- [49] A. Rao, G. Moille, X. Lu, D. A. Westly, D. Sacchetto, M. Geiselman, M. Zervas, S. B. Papp, J. Bowers, and K. Srinivasan, “Towards integrated photonic interposers for processing octave-spanning microresonator frequency combs,” *Light: Science & Applications*, vol. 10, no. 1, p. 109, 2021.
- [50] C. Wang, M. Zhang, M. Yu, R. Zhu, H. Hu, and M. Loncar, “Monolithic lithium niobate photonic circuits for Kerr frequency comb generation and modulation,” *Nature Communications*, vol. 10, no. 1, p. 978, 2019.
- [51] H. Guo, M. Karpov, E. Lucas, A. Kordts, M. H. P. Pfeiffer, V. Brasch, G. Lihachev, V. E. Lobanov, M. L. Gorodetsky, and T. J. Kippenberg, “Universal dynamics and deterministic switching of dissipative Kerr solitons in optical microresonators,” *Nature Physics*, vol. 13, no. 1, pp. 94–102, 2017.

-
- [52] X. Xue, Y. Xuan, P.-H. Wang, Y. Liu, D. E. Leaird, M. Qi, and A. M. Weiner, “Normal-dispersion microcombs enabled by controllable mode interactions,” *Laser & Photonics Reviews*, vol. 9, no. 4, pp. L23–L28, 2015.
- [53] B. Y. Kim, Y. Okawachi, J. K. Jang, M. Yu, X. Ji, Y. Zhao, C. Joshi, M. Lipson, and A. L. Gaeta, “Turn-key, high-efficiency Kerr comb source,” *Optics Letters*, vol. 44, no. 18, pp. 4475–4478, 2019.
- [54] S.-P. Yu, D. C. Cole, H. Jung, G. T. Moille, K. Srinivasan, and S. B. Papp, “Spontaneous pulse formation in edgeless photonic crystal resonators,” *Nature Photonics*, vol. 15, no. 6, pp. 461–467, 2021.
- [55] W. Jin, Q.-F. Yang, L. Chang, B. Shen, H. Wang, M. A. Leal, L. Wu, M. Gao, A. Feshali, M. Paniccia, K. J. Vahala, and J. E. Bowers, “Hertz-linewidth semiconductor lasers using CMOS-ready ultra-high-Q microresonators,” *Nature Photonics*, vol. 15, no. 5, pp. 346–353, 2021.
- [56] D. T. Spencer, T. Drake, T. C. Briles, J. Stone, L. C. Sinclair, C. Fredrick, Q. Li, D. Westly, B. R. Ilic, A. Bluestone, N. Volet, T. Komljenovic, L. Chang, S. H. Lee, D. Y. Oh, M.-G. Suh, K. Y. Yang, M. H. P. Pfeiffer, T. J. Kippenberg, E. Norberg, L. Theogarajan, K. Vahala, N. R. Newbury, K. Srinivasan, J. E. Bowers, S. A. Diddams, and S. B. Papp, “An optical-frequency synthesizer using integrated photonics,” *Nature*, vol. 557, no. 7703, pp. 81–85, 2018.
- [57] L. Chang, W. Xie, H. Shu, Q.-F. Yang, B. Shen, A. Boes, J. D. Peters, W. Jin, C. Xiang, S. Liu, G. Moille, S.-P. Yu, X. Wang, K. Srinivasan, S. B. Papp, K. Vahala, and J. E. Bowers, “Ultra-efficient frequency comb generation in AlGaAs-on-insulator microresonators,” *Nature Communications*, vol. 11, no. 1, p. 1331, 2020.
- [58] C. Bao, L. Zhang, A. Matsko, Y. Yan, Z. Zhao, G. Xie, A. M. Agarwal, L. C. Kimerling, J. Michel, L. Maleki, and A. E. Willner, “Nonlinear conversion efficiency in Kerr frequency comb generation,” *Optics Letters*, vol. 39, no. 21, pp. 6126–6129, 2014.

- [59] X. Xue, P.-H. Wang, Y. Xuan, M. Qi, and A. M. Weiner, “Microresonator Kerr frequency combs with high conversion efficiency,” *Laser & Photonics Reviews*, vol. 11, no. 1, p. 1600276, 2017.
- [60] J. Li, C. Bao, Q.-X. Ji, H. Wang, L. Wu, S. Leifer, C. Beichman, and K. Vahala, “Efficiency of pulse pumped soliton microcombs,” *Optica*, vol. 9, no. 2, p. 231, 2022.
- [61] M. H. Anderson, R. Bouchand, J. Liu, W. Weng, E. Obrzud, T. Herr, and T. J. Kippenberg, “Photonic chip-based resonant supercontinuum via pulse-driven Kerr microresonator solitons,” *Optica*, vol. 8, no. 6, p. 771, 2021.
- [62] H. Bao, A. Cooper, M. Rowley, L. Di Lauro, J. S. Toterogongora, S. T. Chu, B. E. Little, G.-L. Oppo, R. Morandotti, D. J. Moss, B. Wetzels, M. Peccianti, and A. Pasquazi, “Laser cavity-soliton microcombs,” *Nature Photonics*, vol. 13, no. 6, pp. 384–389, 2019.
- [63] A. W. Bruch, X. Liu, Z. Gong, J. B. Surya, M. Li, C.-L. Zou, and H. X. Tang, “Pockels soliton microcomb,” *Nature Photonics*, vol. 15, no. 1, pp. 21–27, 2021.
- [64] X. Xue, X. Zheng, and B. Zhou, “Super-efficient temporal solitons in mutually coupled optical cavities,” *Nature Photonics*, vol. 13, no. 9, pp. 616–622, 2019.
- [65] A. Hasegawa, “An historical review of application of optical solitons for high speed communications,” *Chaos: An Interdisciplinary Journal of Nonlinear Science*, vol. 10, no. 3, pp. 475–485, 2000.
- [66] P. J. Winzer, D. T. Neilson, and A. R. Chraplyvy, “Fiber-optic transmission and networking: the previous 20 and the next 20 years [Invited],” *Optics Express*, vol. 26, no. 18, p. 24190, 2018.
- [67] G. P. Agrawal, *Fiber-Optic Communication Systems*. John Wiley & Sons, Inc., 2010.
- [68] G. P. Agrawal, *Nonlinear Fiber Optics*, 5th ed. Elsevier, 2012.
- [69] R. W. Boyd, *Nonlinear Optics*, 3rd ed. Academic Press, 2008.
- [70] V. P. Tzolov, N. Godbout, S. Lacroix, and M. Fontaine, “Nonlinear self-phase-modulation effects: a vectorial first-order perturbation approach,” *Optics Letters*, vol. 20, no. 5, p. 456, 1995.

-
- [71] J. Hult, "A Fourth-Order Runge–Kutta in the Interaction Picture Method for Simulating Supercontinuum Generation in Optical Fibers," *Journal of Lightwave Technology*, vol. 25, no. 12, pp. 3770–3775, 2007.
- [72] F. Shimizu, "Frequency Broadening in Liquids by a Short Light Pulse," *Physical Review Letters*, vol. 19, no. 19, pp. 1097–1100, 1967.
- [73] A. Hasegawa, "Generation of a train of soliton pulses by induced modulational instability in optical fibers," *Optics Letters*, vol. 9, no. 7, p. 288, 1984.
- [74] A. Hasegawa and F. Tappert, "Transmission of stationary nonlinear optical pulses in dispersive dielectric fibers. I. Anomalous dispersion," *Applied Physics Letters*, vol. 23, no. 3, pp. 142–144, 1973.
- [75] J. S. Russell, "Report of the fourteenth meeting of the British Association for the Advancement of Science," York, 1844 (London 1845), pp. 311–390.
- [76] N. J. Zabusky and M. D. Kruskal, "Interaction of "Solitons" in a Collisionless Plasma and the Recurrence of Initial States," *Physical Review Letters*, vol. 15, no. 6, pp. 240–243, 1965.
- [77] D. J. Korteweg and G. de Vries, "XLI. On the change of form of long waves advancing in a rectangular canal, and on a new type of long stationary waves," *The London, Edinburgh, and Dublin Philosophical Magazine and Journal of Science*, vol. 39, no. 240, pp. 422–443, 1895.
- [78] H. Washimi and T. Taniuti, "Propagation of Ion-Acoustic Solitary Waves of Small Amplitude," *Physical Review Letters*, vol. 17, no. 19, pp. 996–998, 1966.
- [79] A. Scott, F. Chu, and D. McLaughlin, "The soliton: A new concept in applied science," *Proceedings of the IEEE*, vol. 61, no. 10, pp. 1443–1483, 1973.
- [80] "Exact theory of two-dimensional self-focusing and one-dimensional self-modulation of waves in nonlinear media," *Soviet journal of experimental and theoretical physics*, vol. 34, no. 1, p. 62, 1972.

- [81] A. Cazaubiel, G. Michel, S. Lepot, B. Semin, S. Aumaître, M. Berhanu, F. Bonnefoy, and E. Falcon, “Coexistence of solitons and extreme events in deep water surface waves,” *Physical Review Fluids*, vol. 3, no. 11, p. 114802, 2018.
- [82] B. M. Lake, H. C. Yuen, H. Rungaldier, and W. E. Ferguson, “Non-linear deep-water waves: theory and experiment. Part 2. Evolution of a continuous wave train,” *Journal of Fluid Mechanics*, vol. 83, no. 1, pp. 49–74, 1977.
- [83] A. Hasegawa and F. Tappert, “Transmission of stationary nonlinear optical pulses in dispersive dielectric fibers. II. Normal dispersion,” *Applied Physics Letters*, vol. 23, no. 4, pp. 171–172, 1973.
- [84] L. F. Mollenauer, R. H. Stolen, and J. P. Gordon, “Experimental Observation of Picosecond Pulse Narrowing and Solitons in Optical Fibers,” *Physical Review Letters*, vol. 45, no. 13, pp. 1095–1098, 1980.
- [85] A. M. Weiner, J. P. Heritage, R. J. Hawkins, R. N. Thurston, E. M. Kirschner, D. E. Leaird, and W. J. Tomlinson, “Experimental Observation of the Fundamental Dark Soliton in Optical Fibers,” *Physical Review Letters*, vol. 61, no. 21, pp. 2445–2448, 1988.
- [86] J. E. Rothenberg and H. K. Heinrich, “Observation of the formation of dark-soliton trains in optical fibers,” *Optics Letters*, vol. 17, no. 4, p. 261, 1992.
- [87] K. Blow and N. Doran, “The asymptotic dispersion of soliton pulses in lossy fibres,” *Optics Communications*, vol. 52, no. 5, pp. 367–370, 1985.
- [88] J. P. Gordon and H. A. Haus, “Random walk of coherently amplified solitons in optical fiber transmission,” *Optics Letters*, vol. 11, no. 10, p. 665, 1986.
- [89] N. Akhmediev and A. Ankiewicz, *Dissipative Solitons: From Optics to Biology and Medicine*, ser. Lecture Notes in Physics. Berlin, Heidelberg: Springer Berlin Heidelberg, 2008, vol. 751.
- [90] P. Grelu and N. Akhmediev, “Dissipative solitons for mode-locked lasers,” *Nature Photonics*, vol. 6, no. 2, pp. 84–92, 2012.

-
- [91] O. Thual and S. Fauve, “Localized structures generated by subcritical instabilities,” *Journal de Physique*, vol. 49, no. 11, pp. 1829–1833, 1988.
- [92] P. Parra-Rivas and C. Fernandez-Oto, “Formation of localized states in dryland vegetation: Bifurcation structure and stability,” *Physical Review E*, vol. 101, no. 5, p. 052214, 2020.
- [93] T. Sylvestre, S. Coen, P. Emplit, and M. Haelterman, “Self-induced modulational instability laser revisited: normal dispersion and dark-pulse train generation,” *Optics Letters*, vol. 27, no. 7, pp. 482–484, 2002.
- [94] L. F. Mollenauer and R. H. Stolen, “The soliton laser,” *Optics Letters*, vol. 9, no. 1, pp. 13–15, 1984.
- [95] W. Chang, A. Ankiewicz, J. M. Soto-Crespo, and N. Akhmediev, “Dissipative soliton resonances,” *Physical Review A*, vol. 78, no. 2, p. 023830, 2008.
- [96] S. T. Cundiff, J. M. Soto-Crespo, and N. Akhmediev, “Experimental Evidence for Soliton Explosions,” *Physical Review Letters*, vol. 88, no. 7, p. 073903, 2002.
- [97] Y. H. Wen, M. R. E. Lamont, S. H. Strogatz, and A. L. Gaeta, “Self-organization in Kerr-cavity-soliton formation in parametric frequency combs,” *Physical Review A*, vol. 94, no. 6, p. 063843, 2016.
- [98] P. Parra-Rivas, D. Gomila, E. Knobloch, S. Coen, and L. Gelens, “Origin and stability of dark pulse Kerr combs in normal dispersion resonators,” *Optics Letters*, vol. 41, no. 11, pp. 2402–2405, 2016.
- [99] K. J. Vahala, “Optical microcavities,” *Nature*, vol. 424, no. 6950, pp. 839–846, 2003.
- [100] I. Chremmos, O. Schwelb, and N. Uzunoglu, Eds., *Photonic Microresonator Research and Applications*, ser. Springer Series in Optical Sciences. Boston, MA: Springer US, 2010, vol. 156.
- [101] J. Hryniewicz, P. Absil, B. Little, R. Wilson, and P.-T. Ho, “Higher order filter response in coupled microring resonators,” *IEEE Photonics Technology Letters*, vol. 12, no. 3, pp. 320–322, 2000.

- [102] E. Krioukov, D. J. W. Klunder, A. Driessen, J. Greve, and C. Otto, “Sensor based on an integrated optical microcavity,” *Optics Letters*, vol. 27, no. 7, p. 512, 2002.
- [103] Q. Xu, B. Schmidt, S. Pradhan, and M. Lipson, “Micrometre-scale silicon electro-optic modulator,” *Nature*, vol. 435, pp. 325–327, 2005.
- [104] A. Perot and C. Fabry, “On the Application of Interference Phenomena to the Solution of Various Problems of Spectroscopy and Metrology,” *The Astrophysical Journal*, vol. 9, p. 87, 1899.
- [105] L. F. Stokes, M. Chodorow, and H. J. Shaw, “All-single-mode fiber resonator,” *Optics Letters*, vol. 7, no. 6, p. 288, 1982.
- [106] P. Urquhart, “Compound optical-fiber-based resonators,” *Journal of the Optical Society of America A*, vol. 5, no. 6, p. 803, 1988.
- [107] H. Haus and W. Huang, “Coupled-mode theory,” *Proceedings of the IEEE*, vol. 79, no. 10, pp. 1505–1518, 1991.
- [108] A. Yariv, “Universal relations for coupling of optical power between microresonators and dielectric waveguides,” *Electronics Letters*, vol. 36, no. 4, pp. 321–322, 2000.
- [109] W. Bogaerts, P. De Heyn, T. Van Vaerenbergh, K. De Vos, S. Kumar Selvaraja, T. Claes, P. Dumon, P. Bienstman, D. Van Thourhout, and R. Baets, “Silicon microring resonators,” *Laser & Photonics Reviews*, vol. 6, no. 1, pp. 47–73, 2012.
- [110] J. E. Heebner and R. W. Boyd, “Enhanced all-optical switching by use of a nonlinear fiber ring resonator,” *Optics Letters*, vol. 24, no. 12, pp. 847–849, 1999.
- [111] P. Del’Haye, O. Arcizet, M. L. Gorodetsky, R. Holzwarth, and T. J. Kippenberg, “Frequency comb assisted diode laser spectroscopy for measurement of microcavity dispersion,” *Nature Photonics*, vol. 3, pp. 529–533, 2009.
- [112] K. Twayana, Z. Ye, Ó. B. Helgason, K. Vijayan, M. Karlsson, and V. Torres-Company, “Frequency-comb-calibrated swept-wavelength interferometry,” *Optics Express*, vol. 29, no. 15, p. 24363, 2021.

-
- [113] M. H. P. Pfeiffer, J. Liu, A. S. Raja, T. Morais, B. Ghadiani, and T. J. Kippenberg, “Ultra-smooth silicon nitride waveguides based on the Damascene reflow process: fabrication and loss origins,” *Optica*, vol. 5, no. 7, pp. 884–892, 2018.
- [114] T. Herr, K. Hartinger, J. Riemensberger, C. Y. Wang, E. Gavartin, R. Holzwarth, M. L. Gorodetsky, and T. J. Kippenberg, “Universal formation dynamics and noise of Kerr-frequency combs in microresonators,” *Nature Photonics*, vol. 6, no. 7, pp. 480–487, 2012.
- [115] T. Herr, V. Brasch, J. D. Jost, I. Mirgorodskiy, G. Lihachev, M. L. Gorodetsky, and T. J. Kippenberg, “Mode Spectrum and Temporal Soliton Formation in Optical Microresonators,” *Physical Review Letters*, vol. 113, no. 12, p. 123901, 2014.
- [116] A. Arbabi and L. L. Goddard, “Measurements of the refractive indices and thermo-optic coefficients of Si₃N₄ and SiO_x using microring resonances,” *Optics Letters*, vol. 38, no. 19, p. 3878, 2013.
- [117] K. Ikeda, R. E. Saperstein, N. Alic, and Y. Fainman, “Thermal and Kerr nonlinear properties of plasma-deposited silicon nitride/silicon dioxide waveguides,” *Optics Express*, vol. 16, no. 17, pp. 12987–12994, 2008.
- [118] X. Jiang and L. Yang, “Optothermal dynamics in whispering-gallery microresonators,” *Light: Science & Applications*, vol. 9, no. 1, p. 24, 2020.
- [119] X. Xue, Y. Xuan, C. Wang, P.-H. Wang, Y. Liu, B. Niu, D. E. Leaird, M. Qi, and A. M. Weiner, “Thermal tuning of Kerr frequency combs in silicon nitride microring resonators,” *Optics Express*, vol. 24, no. 1, p. 687, 2016.
- [120] M. Bayer, T. Gutbrod, J. P. Reithmaier, A. Forchel, T. L. Reinecke, P. A. Knipp, A. A. Dremin, and V. D. Kulakovskii, “Optical Modes in Photonic Molecules,” *Physical Review Letters*, vol. 81, no. 12, pp. 2582–2585, 1998.
- [121] Y. Liu, A. Choudhary, D. Marpaung, and B. J. Eggleton, “Integrated microwave photonic filters,” *Advances in Optics and Photonics*, vol. 12, no. 2, p. 485, 2020.

- [122] L. Lu, J. D. Joannopoulos, and M. Soljačić, “Topological photonics,” *Nature Photonics* 2014 8:11, vol. 8, no. 11, pp. 821–829, 2014.
- [123] M. A. Bandres, S. Wittek, G. Harari, M. Parto, J. Ren, M. Segev, D. N. Christodoulides, and M. Khajavikhan, “Topological insulator laser: Experiments,” *Science*, vol. 359, no. 6381, 2018.
- [124] S. Mittal, G. Moille, K. Srinivasan, Y. K. Chembo, and M. Hafezi, “Topological frequency combs and nested temporal solitons,” *Nature Physics*, vol. 17, no. 10, pp. 1169–1176, 2021.
- [125] A. Tikan, J. Riemensberger, K. Komagata, S. Hönl, M. Churayev, C. Skehan, H. Guo, R. N. Wang, J. Liu, P. Seidler, and T. J. Kippenberg, “Emergent Nonlinear Phenomena in a Driven Dissipative Photonic Dimer,” *Nature Physics*, vol. 17, no. 5, pp. 604–610, 2020.
- [126] T. Klaassen, J. de Jong, M. van Exter, and J. P. Woerdman, “Transverse mode coupling in an optical resonator,” *Optics Letters*, vol. 30, no. 15, pp. 1959–1961, 2005.
- [127] J. Zhu, S. K. Ozdemir, L. He, and L. Yang, “Controlled manipulation of mode splitting in an optical microcavity by two Rayleigh scatterers,” *Optics Express*, vol. 18, no. 23, pp. 23 535–23 543, 2010.
- [128] S.-W. Huang, H. Liu, J. Yang, M. Yu, D.-L. Kwong, and C. W. Wong, “Smooth and flat phase-locked Kerr frequency comb generation by higher order mode suppression,” *Scientific Reports*, vol. 6, no. 1, p. 26255, 2016.
- [129] C. Bao, Y. Xuan, D. E. Leaird, S. Wabnitz, M. Qi, and A. M. Weiner, “Spatial mode-interaction induced single soliton generation in microresonators,” *Optica*, vol. 4, no. 9, p. 1011, 2017.
- [130] S. A. Miller, Y. Okawachi, S. Ramelow, K. Luke, A. Dutt, A. Farsi, A. L. Gaeta, and M. Lipson, “Tunable frequency combs based on dual microring resonators,” *Optics Express*, vol. 23, no. 16, pp. 21 527–21 540, 2015.
- [131] W.-P. Huang, “Coupled-mode theory for optical waveguides: an overview,” *Journal of the Optical Society of America A*, vol. 11, no. 3, pp. 963–983, 1994.

-
- [132] K. Oda, N. Takato, and H. Toba, “A wide-FSR waveguide double-ring resonator for optical FDM transmission systems,” *Journal of Lightwave Technology*, vol. 9, no. 6, pp. 728–736, 1991.
- [133] S. Pereira, P. Chak, and J. E. Sipe, “All-optical AND gate by use of a Kerr nonlinear microresonator structure,” *Optics Letters*, vol. 28, no. 6, p. 444, 2003.
- [134] N. Moroney, L. D. Bino, M. T. M. Woodley, G. N. Ghalanos, J. M. Silver, A. O. Svela, S. Zhang, and P. Del’Haye, “Logic Gates Based on Interaction of Counterpropagating Light in Microresonators,” *Journal of Lightwave Technology*, vol. 38, no. 6, pp. 1414–1419, 2020.
- [135] T. Carmon and K. J. Vahala, “Visible continuous emission from a silica microphotonic device by third-harmonic generation,” *Nature Physics*, vol. 3, no. 6, pp. 430–435, 2007.
- [136] J. S. Levy, M. A. Foster, A. L. Gaeta, and M. Lipson, “Harmonic generation in silicon nitride ring resonators,” *Optics Express*, vol. 19, no. 12, p. 11415, 2011.
- [137] V. Brasch, E. Lucas, J. D. Jost, M. Geiselmann, and T. J. Kippenberg, “Self-referenced photonic chip soliton Kerr frequency comb,” *Light: Science & Applications*, vol. 6, no. 1, pp. e16 202–e16 202, 2017.
- [138] K. Ikeda, “Multiple-valued stationary state and its instability of the transmitted light by a ring cavity system,” *Optics Communications*, vol. 30, no. 2, pp. 257–261, 1979.
- [139] T. Hansson and S. Wabnitz, “Frequency comb generation beyond the Lugiato–Lefever equation: multi-stability and super cavity solitons,” *Journal of the Optical Society of America B*, vol. 32, no. 7, pp. 1259–1266, 2015.
- [140] V. Torres-Company, D. Castelló-Lurbe, and E. Silvestre, “Comparative analysis of spectral coherence in microresonator frequency combs,” *Optics Express*, vol. 22, no. 4, pp. 4678–4691, 2014.
- [141] J. M. Dudley and S. Coen, “Coherence properties of supercontinuum spectra generated in photonic crystal and tapered optical fibers,” *Optics Letters*, vol. 27, no. 13, pp. 1180–1182, 2002.

- [142] L. A. Lugiato and R. Lefever, “Spatial Dissipative Structures in Passive Optical Systems,” *Physical Review Letters*, vol. 58, no. 21, pp. 2209–2211, 1987.
- [143] M. Haelterman, S. Trillo, and S. Wabnitz, “Dissipative modulation instability in a nonlinear dispersive ring cavity,” *Optics Communications*, vol. 91, no. 5-6, pp. 401–407, 1992.
- [144] S. Coen and M. Erkintalo, “Universal scaling laws of Kerr frequency combs,” *Optics Letters*, vol. 38, no. 11, pp. 1790–1792, 2013.
- [145] I. V. Barashenkov and Y. S. Smirnov, “Existence and stability chart for the ac-driven, damped nonlinear Schrödinger solitons,” *Physical Review E*, vol. 54, no. 5, pp. 5707–5725, 1996.
- [146] C. Godey, I. V. Balakireva, A. Coillet, and Y. K. Chembo, “Stability analysis of the spatiotemporal Lugiato-Lefever model for Kerr optical frequency combs in the anomalous and normal dispersion regimes,” *Physical Review A*, vol. 89, no. 6, p. 063814, 2014.
- [147] P. Parra-Rivas, E. Knobloch, D. Gomila, and L. Gelens, “Dark solitons in the Lugiato-Lefever equation with normal dispersion,” *Physical Review A*, vol. 93, no. 6, p. 063839, 2016.
- [148] T. Hansson, D. Modotto, and S. Wabnitz, “Dynamics of the modulational instability in microresonator frequency combs,” *Physical Review A*, vol. 88, no. 2, p. 023819, 2013.
- [149] S. Coen, H. G. Randle, T. Sylvestre, and M. Erkintalo, “Modeling of octave-spanning Kerr frequency combs using a generalized mean-field Lugiato–Lefever model,” *Optics Letters*, vol. 38, no. 1, p. 37, 2013.
- [150] A. A. Savchenkov, A. B. Matsko, D. Strekalov, M. Mohageg, V. S. Ilchenko, and L. Maleki, “Low Threshold Optical Oscillations in a Whispering Gallery CaF₂ Resonator,” *Physical Review Letters*, vol. 93, no. 24, p. 243905, 2004.
- [151] A. Coillet and Y. Chembo, “On the robustness of phase locking in Kerr optical frequency combs,” *Optics Letters*, vol. 39, no. 6, pp. 1529–1532, 2014.

-
- [152] N. L. B. Sayson, T. Bi, V. Ng, H. Pham, L. S. Trainor, H. G. L. Schwefel, S. Coen, M. Erkintalo, and S. G. Murdoch, “Octave-spanning tunable parametric oscillation in crystalline Kerr microresonators,” *Nature Photonics*, vol. 13, no. 10, pp. 701–706, 2019.
- [153] J. R. Stone, G. Moille, X. Lu, and K. Srinivasan, “Conversion Efficiency in Kerr-Microresonator Optical Parametric Oscillators: From Three Modes to Many Modes,” *Physical Review Applied*, vol. 17, no. 2, p. 024038, 2022.
- [154] S.-W. Huang, J. Yang, S.-H. Yang, M. Yu, D.-L. Kwong, T. Zelevinsky, M. Jarrahi, and C. W. Wong, “Globally Stable Microresonator Turing Pattern Formation for Coherent High-Power THz Radiation On-Chip,” *Physical Review X*, vol. 7, no. 4, p. 041002, 2017.
- [155] M. R. E. Lamont, Y. Okawachi, and A. L. Gaeta, “Route to stabilized ultrabroadband microresonator-based frequency combs,” *Optics Letters*, vol. 38, no. 18, pp. 3478–3481, 2013.
- [156] J. A. Jaramillo-Villegas, X. Xue, P.-H. Wang, D. E. Leaird, and A. M. Weiner, “Deterministic single soliton generation and compression in microring resonators avoiding the chaotic region,” *Optics Express*, vol. 23, no. 8, pp. 9618–9626, 2015.
- [157] Y. Liu, Y. Xuan, X. Xue, P.-H. Wang, S. Chen, A. J. Metcalf, J. Wang, D. E. Leaird, M. Qi, and A. M. Weiner, “Investigation of mode coupling in normal-dispersion silicon nitride microresonators for Kerr frequency comb generation,” *Optica*, vol. 1, no. 3, pp. 137–144, 2014.
- [158] J. K. Jang, Y. Okawachi, M. Yu, K. Luke, X. Ji, M. Lipson, and A. L. Gaeta, “Dynamics of mode-coupling-induced microresonator frequency combs in normal dispersion,” *Optics Express*, vol. 24, no. 25, pp. 28 794–28 803, 2016.
- [159] X. Xue, F. Leo, Y. Xuan, J. A. Jaramillo-Villegas, P.-H. Wang, D. E. Leaird, M. Erkintalo, M. Qi, and A. M. Weiner, “Second-harmonic-assisted four-wave mixing in chip-based microresonator frequency comb generation,” *Light: Science & Applications*, vol. 6, no. 4, pp. e16 253–e16 253, 2017.

- [160] N. M. Kondratiev, V. E. Lobanov, E. A. Lonshakov, N. Y. Dmitriev, A. S. Voloshin, and I. A. Bilenko, “Numerical study of solitonic pulse generation in the self-injection locking regime at normal and anomalous group velocity dispersion,” *Optics Express*, vol. 28, no. 26, p. 38892, 2020.
- [161] A. B. Matsko, A. A. Savchenkov, D. Strekalov, V. S. Ilchenko, and L. Maleki, “Optical hyperparametric oscillations in a whispering-gallery-mode resonator: Threshold and phase diffusion,” *Physical Review A*, vol. 71, no. 3, p. 033804, 2005.
- [162] A. S. Voloshin, N. M. Kondratiev, G. V. Lihachev, J. Liu, V. E. Lobanov, N. Y. Dmitriev, W. Weng, T. J. Kippenberg, and I. A. Bilenko, “Dynamics of soliton self-injection locking in optical microresonators,” *Nature Communications*, vol. 12, no. 1, p. 235, 2021.
- [163] W. Liang, A. A. Savchenkov, V. S. Ilchenko, D. Eliyahu, D. Seidel, A. B. Matsko, and L. Maleki, “Generation of a coherent near-infrared Kerr frequency comb in a monolithic microresonator with normal GVD,” *Optics Letters*, vol. 39, no. 10, pp. 2920–2923, 2014.
- [164] V. Lobanov, G. Lihachev, T. J. Kippenberg, and M. Gorodetsky, “Frequency combs and platicons in optical microresonators with normal GVD,” *Optics Express*, vol. 23, no. 6, pp. 7713–7721, 2015.
- [165] S. Coen, M. Tlidi, P. Emplit, and M. Haelterman, “Convection versus Dispersion in Optical Bistability,” *Physical Review Letters*, vol. 83, no. 12, pp. 2328–2331, 1999.
- [166] C. Bao, J. A. Jaramillo-Villegas, Y. Xuan, D. E. Leaird, M. Qi, and A. M. Weiner, “Observation of Fermi-Pasta-Ulam Recurrence Induced by Breather Solitons in an Optical Microresonator,” *Physical Review Letters*, vol. 117, no. 16, p. 163901, 2016.
- [167] M. Yu, J. K. Jang, Y. Okawachi, A. G. Griffith, K. Luke, S. A. Miller, X. Ji, M. Lipson, and A. L. Gaeta, “Breather soliton dynamics in microresonators,” *Nature Communications*, vol. 8, no. 1, p. 14569, 2017.
- [168] C. Bao, Y. Xuan, C. Wang, A. Fülöp, D. E. Leaird, V. Torres-Company, M. Qi, and A. M. Weiner, “Observation of Breathing

- Dark Pulses in Normal Dispersion Optical Microresonators,” *Physical Review Letters*, vol. 121, no. 25, p. 257401, 2018.
- [169] J. K. Jang, M. Erkintalo, S. G. Murdoch, and S. Coen, “Observation of dispersive wave emission by temporal cavity solitons,” *Optics Letters*, vol. 39, no. 19, p. 5503, 2014.
- [170] C. Milián and D. Skryabin, “Soliton families and resonant radiation in a micro-ring resonator near zero group-velocity dispersion,” *Optics Express*, vol. 22, no. 3, p. 3732, 2014.
- [171] C. Bao, H. Taheri, L. Zhang, A. Matsko, Y. Yan, P. Liao, L. Maleki, and A. E. Willner, “High-order dispersion in Kerr comb oscillators,” *Journal of the Optical Society of America B*, vol. 34, no. 4, p. 715, 2017.
- [172] H. Taheri and A. B. Matsko, “Quartic dissipative solitons in optical Kerr cavities,” *Optics Letters*, vol. 44, no. 12, p. 3086, 2019.
- [173] M. Karpov, H. Guo, A. Kordts, V. Brasch, M. H. P. Pfeiffer, M. Zervas, M. Geiselmann, and T. J. Kippenberg, “Raman Self-Frequency Shift of Dissipative Kerr Solitons in an Optical Microresonator,” *Physical Review Letters*, vol. 116, no. 10, p. 103902, 2016.
- [174] C. Milián, A. V. Gorbach, M. Taki, A. V. Yulin, and D. V. Skryabin, “Solitons and frequency combs in silica microring resonators: Interplay of the Raman and higher-order dispersion effects,” *Physical Review A*, vol. 92, no. 3, p. 033851, 2015.
- [175] Q.-F. Yang, X. Yi, K. Y. Yang, and K. Vahala, “Stokes solitons in optical microcavities,” *Nature Physics*, vol. 13, no. 1, pp. 53–57, 2017.
- [176] T. Tan, Z. Yuan, H. Zhang, G. Yan, S. Zhou, N. An, B. Peng, G. Soavi, Y. Rao, and B. Yao, “Multispecies and individual gas molecule detection using Stokes solitons in a graphene over-modal microresonator,” *Nature Communications*, vol. 12, no. 1, p. 6716, 2021.
- [177] M. Karpov, M. H. P. Pfeiffer, H. Guo, W. Weng, J. Liu, and T. J. Kippenberg, “Dynamics of soliton crystals in optical microresonators,” *Nature Physics*, vol. 15, no. 10, pp. 1071–1077, 2019.

- [178] B. Corcoran, M. Tan, X. Xu, A. Boes, J. Wu, T. G. Nguyen, S. T. Chu, B. E. Little, R. Morandotti, A. Mitchell, and D. J. Moss, "Ultra-dense optical data transmission over standard fibre with a single chip source," *Nature Communications*, vol. 11, no. 1, p. 2568, 2020.
- [179] A. Pasquazi, L. Caspani, M. Peccianti, M. Clerici, M. Ferrera, L. Razzari, D. Duchesne, B. E. Little, S. T. Chu, D. J. Moss, and R. Morandotti, "Self-locked optical parametric oscillation in a CMOS compatible microring resonator: a route to robust optical frequency comb generation on a chip," *Optics Express*, vol. 21, no. 11, p. 13333, 2013.
- [180] W. Weng, A. Kaszubowska-Anandarajah, J. He, P. D. Lakshmi-jayasimha, E. Lucas, J. Liu, P. M. Anandarajah, and T. J. Kippenberg, "Gain-switched semiconductor laser driven soliton microcombs," *Nature Communications*, vol. 12, no. 1, p. 1425, 2021.
- [181] Q.-F. Yang, Q.-X. Ji, L. Wu, B. Shen, H. Wang, C. Bao, Z. Yuan, and K. Vahala, "Dispersive-wave induced noise limits in miniature soliton microwave sources," *Nature Communications*, vol. 12, no. 1, p. 1442, 2021.
- [182] C. M. Gentry, X. Zeng, and M. A. Popović, "Tunable coupled-mode dispersion compensation and its application to on-chip resonant four-wave mixing," *Optics Letters*, vol. 39, no. 19, p. 5689, 2014.
- [183] E. Zhu and C. Zhao, "Modulation instability of Kerr optical frequency combs in dual-coupled optical cavities," *Physical Review A*, vol. 105, no. 1, p. 013524, 2022.
- [184] S. Fujii, Y. Okabe, R. Suzuki, T. Kato, A. Hori, Y. Honda, and T. Tanabe, "Analysis of Mode Coupling Assisted Kerr Comb Generation in Normal Dispersion System," *IEEE Photonics Journal*, vol. 10, no. 5, p. 4501511, 2018.
- [185] H. Wang, Y.-K. Lu, L. Wu, D. Y. Oh, B. Shen, S. H. Lee, and K. Vahala, "Dirac solitons in optical microresonators," *Light: Science & Applications*, vol. 9, no. 1, p. 205, 2020.
- [186] C. Bao, B. Shen, M.-G. Suh, H. Wang, K. Şafak, A. Dai, A. B. Matsko, F. X. Kärtner, and K. Vahala, "Oscillatory motion of a

-
- counterpropagating Kerr soliton dimer,” *Physical Review A*, vol. 103, no. 1, p. L011501, 2021.
- [187] L. Marti, J. P. Vasco, and V. Savona, “Slow-light enhanced frequency combs and dissipative Kerr solitons in silicon coupled-ring microresonators in the telecom band,” *OSA Continuum*, vol. 4, no. 4, p. 1247, 2021.
- [188] N. M. Kondratiev and V. E. Lobanov, “Modulational instability and frequency combs in whispering-gallery-mode microresonators with backscattering,” *Physical Review A*, vol. 101, p. 13816, 2020.
- [189] C. Milián, Y. V. Kartashov, D. V. Skryabin, and L. Torner, “Cavity solitons in a microring dimer with gain and loss,” *Optics Letters*, vol. 43, no. 5, p. 979, 2018.
- [190] Y. Dumeige and P. Féron, “Dispersive tristability in microring resonators,” *Physical Review E*, vol. 72, no. 6, p. 066609, 2005.
- [191] A. Fulop, P.-H. Wang, Y. Xuan, D. E. Leaird, M. Qi, P. A. Andrekson, A. M. Weiner, and V. Torres-Company, “Active feedback stabilization of normal-dispersion microresonator combs,” in *2017 Conference on Lasers and Electro-Optics Europe & European Quantum Electronics Conference (CLEO/Europe-EQEC)*, vol. Part F82-C. IEEE, 2017, pp. 1–1.
- [192] X. Yi, Q.-F. Yang, K. Youl Yang, and K. Vahala, “Active capture and stabilization of temporal solitons in microresonators,” *Optics Letters*, vol. 41, no. 9, p. 2037, 2016.

REFERENCES
